

Synchrotron Self-Compton as a Likely Mechanism of Photons beyond the Synchrotron Limit in GRB 190114C

N. Fraija 1 N. Fraija 1 N. Fraija 2 N. Barniol Duran S. Dichiara 3,4, and P. Beniamini 5 N. Fraija 4 Nacional Autónoma de México, Apdo. Postal 70-264, Cd. Universitaria, México DF 04510, Mexico; nifraija@astro.unam.mx Department of Physics and Astronomy, California State University, Sacramento, 6000 J Street, Sacramento, CA 95819-6041, USA Department of Astronomy, University of Maryland, College Park, MD 20742-4111, USA 4 Astrophysics Science Division, NASA Goddard Space Flight Center, 8800 Greenbelt Rd, Greenbelt, MD 20771, USA Department of Physics, The George Washington University, Washington, DC 20052, USA Received 2019 July 15; revised 2019 August 20; accepted 2019 August 24; published 2019 October 1

Abstract

GRB 190114C, a long and luminous burst, was detected by several satellites and ground-based telescopes from radio wavelengths to GeV gamma-rays. In the GeV gamma-rays, the *Fermi* Large Area Telescope detected 48 photons above 1 GeV during the first 100 s after the trigger time, and the MAGIC telescopes observed for more than 1000 s very high-energy (VHE) emission above 300 GeV. Previous analysis of the multi-wavelength observations showed that, although these are consistent with the synchrotron forward-shock model that evolves from a stratified stellar-wind to a homogeneous ISM-like medium, photons above a few GeV can hardly be interpreted in the synchrotron framework. In the context of the synchrotron forward-shock model, we derive the light curves and spectra of the synchrotron self-Compton (SSC) model in a stratified and homogeneous medium. In particular, we study the evolution of these light curves during the stratified-to-homogeneous afterglow transition. Using the best-fit parameters reported for GRB 190114C we interpret the photons beyond the synchrotron limit in the SSC framework and model its spectral energy distribution. We conclude that low-redshift gamma-ray bursts described under a favorable set of parameters as found in the early afterglow of GRB 190114C could be detected at hundreds of GeV, and also afterglow transitions would allow that VHE emission could be observed for longer periods.

Unified Astronomy Thesaurus concepts: Gamma-ray bursts (629); Non-thermal radiation sources (1119); Astrophysical processes (104); High energy astrophysics (739); Particle physics (2088); Interstellar medium wind (848)

1. Introduction

Gamma-ray bursts (GRBs) are the most luminous explosions in the universe, and one of the most promising sources for multimessenger observation of non-electromagnetic signals such as very high-energy (VHE) neutrinos, cosmic rays, and gravitational waves. Observation of sub-TeV photons from bursts would provide crucial information on GRB physics including hadronic and/or leptonic contributions, values of the bulk Lorentz factors, as well as microphysical parameters. In the *Fermi* Large Area Telescope (LAT) era, detections of bursts linked to GeV photons have been pivotal in painting a comprehensive picture of GRBs.

Recently, Ajello et al. (2019) reported the second Fermi-LAT catalog which summarized the temporal and spectral properties of the 169 GRBs with high-energy photons above 100 MeV detected from 2008 to 2018. Among the highestenergy photons associated (with high probability >0.9) with these bursts are: a 31.31 GeV photon arriving at 0.83 s after the trigger, a 33.39 GeV photon at 81.75 s, and a 19.56 GeV photon at 24.83 s, which were located around GRB 090510, GRB 090902B, and GRB 090926A, respectively. Besides this list, GRB 130427A presented the highest-energy photons ever detected, 73 GeV and 95 GeV, observed at 19 s and 244 s, respectively (Ackermann et al. 2014), and GRB 160509A was related to a 52 GeV photon at 77 s after the trigger (Longo et al. 2016). These bursts exhibited two crucial similarities: (i) the first high-energy photon (≥100 MeV) was delayed with the onset of the prompt phase that was usually reported in the range of hundreds of keV, and (ii) the high-energy emission was

temporarily extended, with a duration much longer than the prompt emission, which was typically less than $\sim\!30\,\mathrm{s}$.

In the range of GeV and harder, VHE emission is expected from the nearest and the brightest bursts. Alternative mechanisms to synchrotron radiation have been widely explored at internal as well as external shocks to interpret this emission. Using hadronic models, photo-hadronic interactions (Dermer et al. 2000; Asano et al. 2009; Fraija 2014) and inelastic proton-neutron collisions (Mészáros & Rees 2000) have been proposed. However, the non-temporal coincidence between GRBs and neutrinos reported by the IceCube collaboration has suggested that the number of hadrons is sufficiently low that hadronic interactions are non-efficient processes (Abbasi et al. 2012; Aartsen et al. 2016, 2015). Using leptonic models, external inverse Compton (IC; Papathanassiou & Meszaros 1996; Panaitescu & Mészáros 2000; Fraija & Veres 2018) and synchrotron self-Compton (SSC; Wang et al. 2001; Zhang & Mészáros 2001; Fraija et al. 2012, 2019a, 2019b, 2019d, 2019e, 2019f; Sacahui et al. 2012; Veres & Mészáros 2012) scenarios have been explored. Therefore, photons with energies higher than 5–10 GeV as detected before (Hurley et al. 1994) and during the Fermi-LAT era (Abdo et al. 2009b; Ackermann et al. 2013, 2014, and references therein) could be evidence of the existence of IC scattering. Several authors have taken into account the two crucial similarities found in the Fermi-LAT light curves and have concluded that VHE emission has its origin in external shocks (Kumar & Barniol Duran 2009, 2010; Zou et al. 2009; Ghisellini et al. 2010; Nava et al. 2014; Fraija et al. 2016b). In particular, Wang et al. (2013) showed that 10–100 GeV photons detected after the prompt phase could have originated by SSC emission of the early afterglow. In the context of external shocks, and requiring observations at other wavelengths, several LAT-detected bursts have been described reaching similar conclusions (Liu et al. 2013; Beniamini et al. 2015; Fraija et al. 2016a).

For the first time, an excess of gamma-ray events with a significance of 20σ during the first 20 min and photons with energies higher than 300 GeV were recently reported by the MAGIC collaboration from GRB 190114C (Mirzoyan et al. 2019). This burst triggered the Burst Area Telescope (BAT) instrument onboard the Swift satellite at 2019 January 14 20:57:06.012 UTC (trigger 883832) (Gropp et al. 2019) and it was followed up by the Gamma-Ray Burst Monitor (GBM; Kocevski et al. 2019), by LAT (Kocevski et al. 2019), by the X-ray Telescope (XRT; Gropp et al. 2019; Osborne et al. 2019), by the Ultraviolet/Optical Telescope (Gropp et al. 2019; Siegel et al. 2019), by the SPI-ACS instrument (Minaev & Pozanenko 2019), by the Mini-CALorimeter instrument (Ursi et al. 2019), by the Hard X-ray Modulation Telescope instrument (Xiao et al. 2019), by Konus-Wind (Frederiks et al. 2019), by the Atacama Large Millimeter/submillimeter Array (ALMA), by the Very Large Array (Laskar et al. 2019) and by several optical telescopes (Alexander et al. 2019; Bolmer & Shady 2019; D'Avanzo et al. 2019; Im et al. 2019a, 2019b; Izzo et al. 2019; Lipunov et al. 2019; Mazaeva et al. 2019; Mirzoyan et al. 2019; Selsing et al. 2019; Tyurina et al. 2019).

Ravasio et al. (2019) analyzed the GBM data and found a typical prompt emission for the first $\sim 4 \, \text{s}$, a smoothly broken power-law (PL) spectrum. However, the GBM data for $\gtrsim 4 \,\mathrm{s}$ showed that (i) the spectral evolution was consistent with a single component similar to that of the LAT spectrum and (ii) the time of the bright peak coincided with the peak exhibited in the LAT data. They concluded that both emissions were originated during the afterglow phase. Similarly, Wang et al. (2019b) analyzed the GBM and LAT data, finding that the MeV and GeV emission of GRB 190114C had the same origin during the afterglow evolution. Using the standard SSC model in a homogeneous medium, Wang et al. (2019a) described the broadband spectral energy distribution (SED) of GRB 190114C during the first 150 s after the trigger time. These authors concluded that the detection of the energetic photons at hundreds of GeV was due to the large burst energy and low redshift. Derishev & Piran (2019) argued that these photons were produced by the Comptonization of X-ray photons.

Fraija et al. (2019c) analyzed the gamma-ray (LAT and GBM), X-ray (BAT and XRT), optical (several telescopes), and radio (ALMA) light curves of GRB 190114C. They showed that the multi-wavelength observations during the first \sim 400 s were consistent with the external shock model evolving in a stratified stellar-wind-like medium and after this time were consistent with a uniform ISM-like medium. They also reported the external shock parameters they found using the Markov chain Monte Carlo (MCMC) method when modeling the multi-wavelength (from radio to Fermi-LAT) data. Moreover, these authors argued that the high-energy photons were produced in the deceleration phase and that an alternative mechanism originating in the forward shocks should be considered to properly describe the photons with energies beyond the synchrotron limit. In particular, the specific model that transitions from stratified stellar wind to a homogeneous ISM was chosen because the synchrotron seed photons

for Comptonization can reproduce the multi-wavelength observations, and also the VHE photons detected for almost 20 min by the MAGIC telescope, which covered the time lapse before and after this transition. It is worth noting that, before this transition, as suggested by some authors (e.g., see Fraija et al. 2019c; Ravasio et al. 2019; Wang et al. 2019b), the LAT, GBM, X-ray, and optical observations are consistent with the evolution of the wind medium afterglow model, and after this transition the X-ray and optical observations are consistent with the constant medium afterglow model (e.g., see Fraija et al. 2019c; Wang et al. 2019a). Motivated by these results, we extend the work of Fraija et al. (2019c) and derive, in this paper, the SSC light curves and spectra in a stratified stellar-wind medium, which transitions to a homogeneous interstellar medium. The paper is organized as follows. In Section 2 we show SSC light curves generated in the forward shock when the outflow decelerates in a stratified stellarwind and homogeneous ISM-like medium. In Section 3 we apply the SSC model to estimate the VHE emission of GRB 190114C using the parameters reported in Fraija et al. (2019c) and also discuss the results. In Section 4, conclusions are presented.

2. SSC Scenario of Forward Shocks

It is widely accepted that the standard synchrotron forwardshock model has been successful in describing the multiwavelength (X-ray, optical, and radio) observations in GRB afterglows. However, relativistic electrons are also expected to be cooled down by SSC emission (e.g., Sari & Esin 2001). We do not discuss the effects of the self-absorption frequency, since it is typically relevant at low energies compared to the GeV energy range (e.g., see Panaitescu et al. 2014). We do not use the reverse-shock emission because it was used in Fraija et al. (2019c) to explain the short-lasting Fermi-LAT and GBM peaks at ~8 s and it cannot describe an emission much longer than this timescale. Due to the absence of neutrinos spatially or temporally associated with GRB 190114C (Vandenbroucke 2019), we neglect more complex models like hadronic or photohadronic processes (Asano et al. 2009; Fraija 2014). They are by no means disfavored by these arguments.

The SSC forward-shock model varies the temporal and spectral features of GRB afterglows significantly and can also explain the gamma-rays above the well-known synchrotron limit (e.g., Abdo et al. 2009a; Piran & Nakar 2010; Barniol Duran & Kumar 2011; Fraija et al. 2019c). The SSC emission of a decelerating outflow moving through either a stratified or homogeneous medium is calculated in the next section.

2.1. SSC Light Curves in the Stratified Stellar-wind Medium

When the outflow interacts with the stratified medium with density $\rho(r)=A\,r^{-2}$, where $A=\frac{\dot{M}}{4\pi\nu_{\rm W}}$, the minimum and the cooling electron Lorentz factors can be written as

$$\gamma_{\rm m} = 5.3 \times 10^2 \, g(p) \, \varepsilon_{e,-2} \, \Gamma_{2.5},$$

$$\gamma_{\rm c} = 2.1 \times 10^5 \left(\frac{1 + Y_{\rm Th}}{3} \right)^{-1} \, \xi^2 \, \varepsilon_{\rm B,-4}^{-1} \, A_{\rm W,-1}^{-2} \, \Gamma_{2.5}^{-3} \, E_{53.5}, \quad (1)$$

respectively. Hereafter, we adopt the convention $Q_x = Q/10^x$ in c.g.s. units. The microphysical parameters ε_B and ε_e correspond to the fraction of the shocked energy density transferred to the magnetic field and electrons, respectively, the

 $[\]dot{M}$ is the mass-loss rate and v is the velocity of the outflow.

equivalent kinetic energy E is associated with the isotropic energy $E_{\gamma,\rm iso}$ and the kinetic efficiency $\eta=E_{\gamma,\rm iso}/E$ which is defined as the fraction of the kinetic energy radiated into gamma-rays, $Y_{\rm Th}$ is the Compton parameter (Sari & Esin 2001; Wang et al. 2010), ξ is a constant parameter of order unity (Chevalier & Li 2000), $g(p)=\frac{p-2}{p-1}\simeq 0.23$ for p=2.3, Γ is the bulk Lorentz factor, and $A_{\rm W}=A/(5\times 10^{11}~{\rm g~cm}^{-1})$ is the parameter of wind density (Dai & Lu 1998; Chevalier & Li 2000; Panaitescu & Kumar 2000; Vink et al. 2000; Chevalier et al. 2004; Vink & de Koter 2005).

Given the hydrodynamic forward-shock evolution in the stratified medium $\Gamma \sim 258.3 \left(\frac{1+z}{1.5}\right)^{\frac{1}{4}} E_{53.5}^{\frac{1}{4}} A_{W,-1}^{-\frac{1}{4}} t_2^{-\frac{1}{4}}$ and the photon energy radiated by the synchrotron process $\epsilon_{\gamma}(\gamma_e) \propto \Gamma B' \gamma_e^2$ with B' the comoving magnetic field, the synchrotron spectral breaks and the maximum flux evolve as $\epsilon_{\rm m}^{\rm syn} \propto t^{-\frac{3}{2}}$, $\epsilon_{\rm c}^{\rm syn} \propto t^{\frac{1}{2}}$ and $F_{\rm max}^{\rm syn} \propto t^{-\frac{1}{2}}$, respectively (Panaitescu & Kumar 2000).

Photons generated by synchrotron radiation can be up-scattered in the forward shocks by the same electron population as $\epsilon_{\mathrm{m(c)}}^{\mathrm{ssc}} \sim \gamma_{\mathrm{m(c)}}^2 \epsilon_{\mathrm{m(c)}}^{\mathrm{syn}}$ with a maximum flux given by $F_{\mathrm{max}}^{\mathrm{ssc}} \sim k\tau F_{\mathrm{max}}^{\mathrm{syn}}$, where τ is the optical depth and $k = \frac{4(p-1)}{p-2}$. Therefore, taking into account the electron Lorentz factors (Equation (1)) and the synchrotron spectral breaks (Chevalier & Li 2000), the SSC spectral breaks and the maximum flux for SSC emission can be written as

$$\epsilon_{\rm m}^{\rm ssc} \simeq 15.1 \text{ keV} g(p)^4 \left(\frac{1+z}{1.5}\right) \xi^{\frac{1}{2}} \varepsilon_{e,-2}^4 \varepsilon_{\rm B,-4}^{\frac{1}{2}} A_{\rm W,-1}^{-\frac{1}{2}} E_{53.5} t_2^{-2},$$

$$\epsilon_{\rm c}^{\rm ssc} \simeq 97.5 \text{ TeV} \left(\frac{1+z}{1.5}\right)^{-3} \left(\frac{1+Y_{\rm Th}}{3}\right)^{-4} \xi^{\frac{9}{2}} \varepsilon_{\rm B,-4}^{-\frac{7}{2}} A_{\rm W,-1}^{-\frac{9}{2}}$$

$$\times E_{53.5} t_2^2,$$

$$F_{\rm max}^{\rm ssc} \simeq 1.1 \times 10^{-4} \text{ mJy} \left(\frac{1+z}{1.5}\right)^2 \xi^{-\frac{5}{2}} \varepsilon_{\rm B,-4}^{\frac{1}{2}} A_{\rm W}^{\frac{5}{2}} D_{27}^{-2} t_2^{-1},$$
(2)

where z=0.5 is the redshift and D is the luminosity distance of the burst. The luminosity distance is obtained using the values of cosmological parameters reported in Planck Collaboration et al. (2018): the matter density parameter $\Omega_{\rm m}=0.315\pm0.007$ and the Hubble constant $H_0=67.4\pm0.5~{\rm km\,s^{-1}\,Mpc^{-1}}$.

During the deceleration phase the intrinsic attenuation by e^{\pm} pair production due to collision of a VHE photon with a lower-energy photon is given by (e.g., see Vedrenne & Atteia 2009)

$$\tau_{\gamma\gamma,\text{in}} \simeq 10^{-2} R_{\text{dec},17} \Gamma_{2.5}^{-1} n_{\gamma,10.8},$$
 (3)

where $R_{\rm dec}=1.17\times 10^{17}\,{\rm cm}\Big(\frac{1+z}{1.5}\Big)^{\frac{1}{2}}\,\xi\,A_{-1}^{-\frac{1}{2}}\,E_{53.5}^{\frac{1}{2}}\,t_2^{\frac{1}{2}}$ is the deceleration radius and $n_\gamma\simeq 6\times 10^{10}\,{\rm cm}^{-3}\,L_{\gamma,50}\,R_{{\rm dec},17}^{-2}\,\Gamma_{2.5}^{-1}$ $\epsilon_{\gamma,3}^{-1}$ is the keV-photon density ($\epsilon_{\gamma,3}=1\,{\rm keV}$) with L_γ the keV-photon luminosity. Since $\tau_{\gamma\gamma,{\rm in}}\ll 1$ during the deceleration phase, the intrinsic attenuation (opacity) is not considered.

Given the SSC spectra for the fast- and slow-cooling regimes together with the SSC spectral breaks and the maximum flux (Equation (2)), the SSC light curves in the fast- (slow)-cooling

regimes are

$$F_{\nu}^{\text{ssc}} = \begin{cases} F_{1,f(s)}^{\text{W}} t_{2}^{-\frac{5}{3}} (t_{2}^{-\frac{1}{3}}) \epsilon_{\gamma,11}^{\frac{1}{3}}, & \epsilon_{\gamma} < \epsilon_{\text{c}}^{\text{ssc}} (\epsilon_{\text{m}}^{\text{ssc}}), \\ F_{2,f(s)}^{\text{W}} t_{2}^{0} \epsilon_{\gamma,11}^{-\frac{1}{2}} (t_{2}^{-p} \epsilon_{\gamma,11}^{-\frac{p-1}{2}}), & \epsilon_{\text{c}}^{\text{ssc}} (\epsilon_{\text{m}}^{\text{ssc}}) < \epsilon_{\gamma} < \epsilon_{\text{m}}^{\text{ssc}} (\epsilon_{\text{c}}^{\text{ssc}}), \\ F_{3,f(s)}^{\text{W}} t_{2}^{1-p} \epsilon_{\gamma,11}^{-\frac{p}{2}}, & \{\epsilon_{\text{m}}^{\text{ssc}}, \epsilon_{\text{c}}^{\text{ssc}}\} < \epsilon_{\gamma}, \end{cases}$$

$$(4)$$

where $\epsilon_{\gamma,11}=100\,\mathrm{GeV}$ and $t_2=100\,\mathrm{s}$ correspond to the energy band and timescale at which the flux is estimated. The values of the proportionality constants $F_{\mathrm{m,n}}^{\mathrm{W}}$ for m=1,2, and 3 and $n=\mathrm{f}$ (fast) or s (slow) are reported in the Appendix. The SSC light curves agree with those derived in Panaitescu & Kumar (2000) for a stratified medium. It is worth noting that these authors calculated the light curves for the energy band of X-rays and timescales of days.

In the SSC spectrum, the Klein–Nishina (KN) regime must be considered because the emissivity beyond this frequency is drastically decreased compared with the classical Thomson regime. The spectral break caused by the decrease of the scattering cross section, due to the KN effect, is given by

$$\epsilon_{\text{KN}}^{\text{ssc}} \simeq 8.8 \text{ TeV} \left(\frac{1+z}{1.5}\right)^{-\frac{3}{2}} \left(\frac{1+Y_{\text{Th}}}{3}\right)^{-1} \xi^2 \varepsilon_{\text{B},-4}^{-1} A_{\text{W},-1}^{-\frac{3}{2}} \times E_{53.5}^{\frac{1}{2}} t_2^{\frac{1}{2}}.$$
 (5)

The SSC light curves given in Equation (4) show two features. (i) The second PL segment of the fast-cooling regime $(\epsilon_c^{\rm ssc} < \epsilon_\gamma < \epsilon_m^{\rm ssc})$ does not evolve with time, and others decrease gradually. This indicates that SSC emission is more likely to be detected during the first seconds after the trigger time. (ii) The first PL segment in the fast-cooling regime $(\epsilon_\gamma < \epsilon_c^{\rm ssc})$, and the third PL segments $(\{\epsilon_m^{\rm ssc}, \epsilon_c^{\rm ssc}\} < \epsilon_\gamma)$ are decaying functions of the circumburst density. This suggests that, depending on the timescale and energy range observed, the SSC emission could be detected in environments with higher and/or lower densities.

The top panels in Figure 1 show the resulting light curves and SEDs of the SSC forward-shock emission generated by a decelerating outflow in a stratified medium. These panels were obtained using relevant values for GRB afterglows. The observable quantities, the microphysical parameters, the parameter density, and the efficiencies are in the range proposed to produce GeV photons in the afterglow phase (e.g., see Beniamini et al. 2015, 2016). The effect of the extragalactic background light (EBL) absorption proposed by Franceschini & Rodighiero (2017) was used. The gold and blue solid curves in the left-hand panel correspond to 10 and 100 GeV, respectively, and the gold and blue dashed-dotted curves to the Fermi-LAT (Piron 2016) and the MAGIC (Takahashi et al. 2008) sensitivities at the same energies, respectively. The purple and green curves in the top right-hand panel correspond to the SEDs at 10 and 100 s, respectively.

The top panels show that the SSC flux is very sensitive to the external density. The light curves above the LAT and MAGIC sensitivities are obtained with $A_{\rm W} = 10^{-1}$ and below with

 $[\]overline{{}^7}$ $E=5 \times 10^{53} \, {\rm erg}, \; p=2.3, \; \varepsilon_{\rm B}=10^{-3}, \; \varepsilon_e=10^{-2}, \; z=0.5, \; \xi=1 \; {\rm and} \; A_{\rm W}=10^{-3} \; (10^{-1})$ for the purple (green) curve.

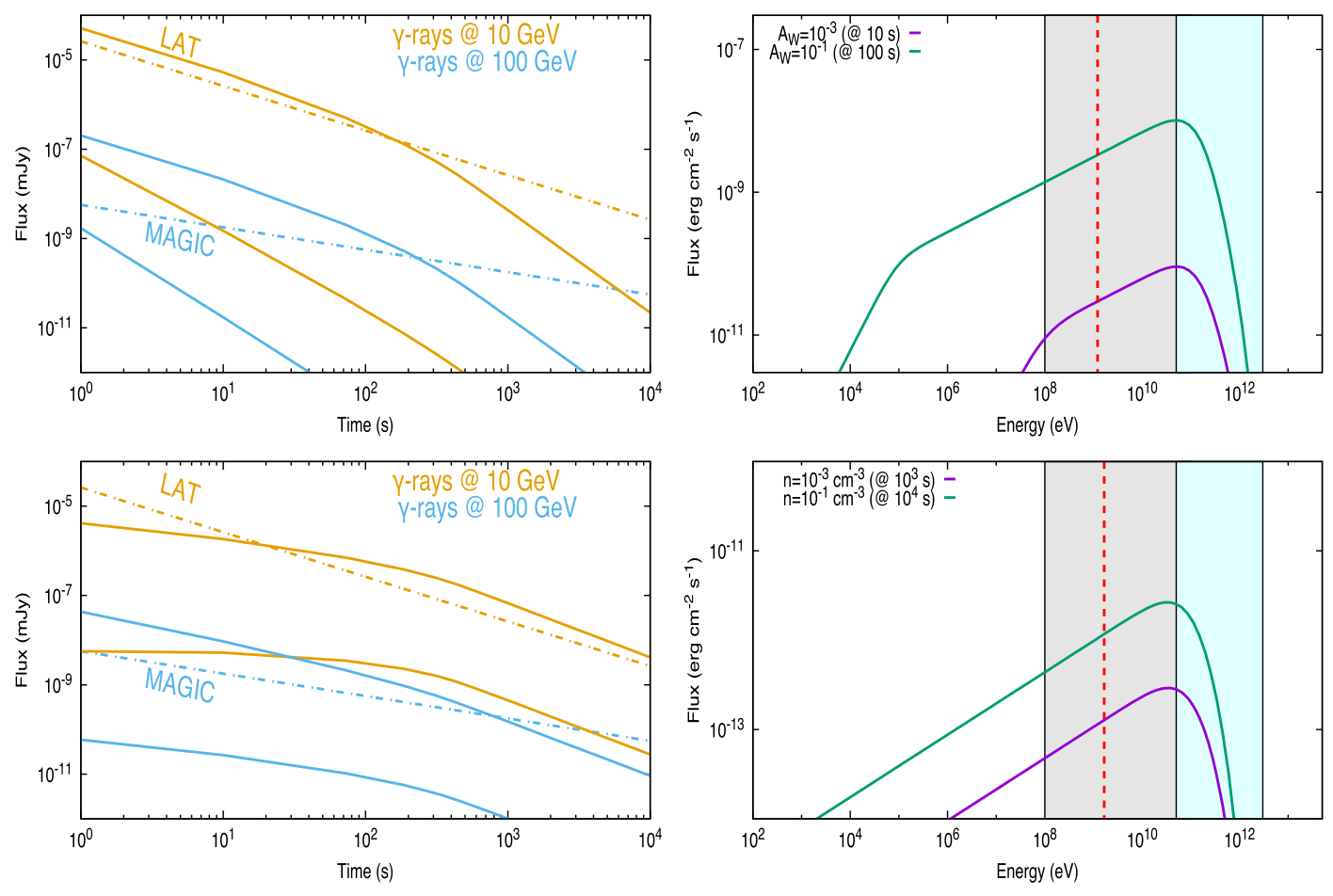


Figure 1. Light curves (left) and SEDs (right) of SSC emission expected from a decelerating outflow in a stratified (above) and homogeneous (below) medium for values of $A_{\rm W}=10^{-3}~(10^{-1})$ and $n=10^{-3}~(10^{-1})$ cm⁻³, respectively. In all panels the values of $E=5\times10^{53}$ erg, p=2.3, $\varepsilon_{\rm B}=10^{-3}$, $\varepsilon_{\rm e}=10^{-2}$ and z=0.5 were used. Dashed-dotted lines in left panels represent the LAT (gold; Piron 2016) and MAGIC (blue; Takahashi et al. 2008) sensitivities at 10 and 100 GeV respectively. The light curves above the LAT and MAGIC sensitivities are obtained with $A_{\rm W}=10^{-1}$ and $n=10^{-1}$ cm⁻³ for a stratified and homogeneous medium, and below the sensitivities are obtained with $A_{\rm W}=10^{-3}$ and $n=10^{-3}$ cm⁻³, respectively. The SEDs are shown at two different times, t=10 and 100 s for the wind medium, and $t=10^{-3}$ and $t=10^{-3}$ and $t=10^{-3}$ cm⁻³, respectively. The self-set of the synchrotron limit. The filled areas in gray and cyan colors correspond to the Fermi-LAT and MAGIC energy ranges, respectively. The effect of the extragalactic background light absorption proposed by Franceschini & Rodighiero (2017) was used.

 $A_{\rm W} = 10^{-3}$. In this particular case, both light curves (at 10 and 100 GeV) evolve in the second PL segment of the slow-cooling regime. The spectral breaks are $\epsilon_{\rm m}^{\rm ssc}=0.5$ MeV and $\epsilon_{\rm c}^{\rm ssc}=2.8\times10^8$ TeV for $A_{\rm W}=10^{-3}$, and $\epsilon_{\rm m}^{\rm ssc}=47.5$ keV and $\epsilon_{\rm c}^{\rm ssc}=0.2$ TeV for $A_{\rm W}=0.1$. The transition times between the fast-to slow-cooling regimes are 0.03 s and 0.3 s for $A_{\rm W}=10^{-3}$ and 0.1, respectively. This shows that with these parameters the SSC emission decreases monotonically with time and increases as the density of the circumburst medium increases. For the chosen parameters, the break energies in the KN regime are $1.2\times10^3\,\mathrm{TeV}$ and $1.3\,\mathrm{TeV}$ for $A_\mathrm{W}=10^{-3}$ and 0.1, respectively, which are above the energies of the Fermi-LAT and MAGIC sensitivities. We emphasize that, depending on the parameter values, the SSC emission would lie in the KN regime, and then this emission would be drastically suppressed. Similarly, the electron distribution that up-scatters synchrotron forward-shock photons beyond the KN regime would be affected (Nakar et al. 2009; Wang et al. 2010) and also the degree of cooling of synchrotron emitting electrons would be affected by KN (Beniamini et al. 2015).

The top left-hand panel of Figure 1 shows that the SSC flux is above the *Fermi-LAT* and MAGIC sensitivities during the

first 100 s for $A_{\rm W}=0.1$ but not for the value of $A_{\rm W}=10^{-3}$. Therefore, the probability to observe the SSC emission from the GRB afterglow is higher during the first seconds after the burst trigger than at late times, and when the stellar wind ejected by the progenitor is denser.

The top right-hand panel shows the SEDs for the same set of parameters at t=10 and $100\,\mathrm{s}$. The value of $A_\mathrm{W}=0.1$ corresponds to the curve above the *Fermi*-LAT and MAGIC sensitivities and the value of $A_\mathrm{W}=10^{-3}$ to the curve below the sensitivities. The red dashed line corresponds to the maximum energy radiated by the synchrotron. The filled areas in gray and cyan colors correspond to the *Fermi*-LAT and MAGIC energy ranges, respectively. The *Fermi*-LAT and MAGIC areas show that photons above the synchrotron limit can be explained by SSC emission. In addition, the top right-hand panel displays that the maximum SSC flux, due to EBL absorption, lies at (i) the end of the LAT energy range where this instrument has less sensitivity (Funk & Hinton 2013) and (ii) the beginning of the MAGIC energy range, making this telescope ideal for detecting the SSC emission.

In order to compare the synchrotron and SSC fluxes at Fermi-LAT energies (e.g., $\epsilon_{\gamma} = 800 \,\text{MeV}$), we obtain the

synchrotron and SSC spectral breaks at $t=10^2 \, \mathrm{s}$ for $A_{\mathrm{W}}=0.1$ ($\epsilon_{\mathrm{m}}^{\mathrm{syn}}=0.2 \, \mathrm{eV}$, $\epsilon_{\mathrm{c}}^{\mathrm{syn}}=0.3 \, \mathrm{keV}$ $\epsilon_{\mathrm{m}}^{\mathrm{ssc}}=47.5 \, \mathrm{keV}$ $\epsilon_{\mathrm{c}}^{\mathrm{ssc}}=0.2 \, \mathrm{TeV}$). Therefore, at the *Fermi*-LAT energy range the synchrotron emission evolves in the third PL segment of the slow-cooling regime and SSC emission in the second PL segment. In this case, the ratio of synchrotron and SSC fluxes becomes

$$\frac{F_{\nu}^{\text{syn}}}{F_{\nu}^{\text{ssc}}} \sim 1.6 \left(\frac{1+z}{1.5}\right)^{\frac{1}{4}} \xi^{\frac{7}{2}} \left(\frac{1+Y_{\text{Th}}}{2}\right)^{-1} \varepsilon_{e,-2}^{-p+\frac{1}{4}} A_{\text{W},-1}^{-\frac{5}{2}} E_{53.5}^{\frac{3}{4}}
\Gamma_{2.5}^{1-p} t_{2}^{\frac{3}{4}} \left(\frac{\epsilon_{\gamma}}{800 \text{ MeV}}\right)^{-\frac{1}{2}},$$
(6)

which is of order unity. Here, we use a smaller value of the effective Compton Y parameter because electrons radiating synchrotron at these large energies have a Compton Y parameter smaller than the corresponding value in the Thomson regime. We can conclude that below $\sim 300 \, \text{MeV}$ the flux can be described in the synchrotron forward-shock scenario, between ~ 0.5 and 1 GeV the contribution of both processes would be relevant, and beyond the synchrotron limit the observations would be entirely explained by the SSC process for this set of parameters.

The top right-hand panel shows that the maximum SSC flux lies at 100 GeV, making it possible to detect the VHE emission in observatories where the sensitivity is maximum at hundreds of GeV (e.g., MAGIC) but not in those observatories where the maximum sensitivity lies in few TeVs (e.g., High Altitude Water Cerenkov (HAWC); Abeysekara et al. 2012). For instance, the SSC flux at 1 TeV decreases between two and three orders of magnitude in comparison with the flux at 100 GeV.

Given the minimum and cooling electron Lorentz factors (Equation (1)), the synchrotron and SSC luminosity ratio can be computed as

$$\frac{L_{\nu}^{\text{ssc}}}{L_{\nu}^{\text{syn}}} \simeq 0.41 \, A_{\text{W},-1} \, R_{\text{dec},17}^{-1} \gamma_{\text{c},5}^2 \left(\frac{\gamma_{\text{c},5}}{\gamma_{\text{m},2}} \right)^{1-p}. \tag{7}$$

It is worth mentioning that the synchrotron and SSC luminosity ratio depends on Y through $\gamma_{\rm c}$. Therefore, in the case of a stratified medium, half of the synchrotron luminosity is upscattered by SSC emission.

2.2. SSC Light Curves in a Homogeneous ISM-like Medium

When the outflow interacts with a homogeneous medium with density n, the minimum and the cooling electron Lorentz

factors can be written as

$$\gamma_{\rm m} = 4.3 \times 10^2 \, g(p) \, \varepsilon_{\rm e} \, \Gamma_2,$$

$$\gamma_{\rm c} = 1.9 \times 10^4 \left(\frac{1 + Y_{\rm Th}}{1.5}\right)^{-1} \left(\frac{1 + z}{2.5}\right) \varepsilon_{\rm B, -4}^{-1} \, n^{-1} \, \Gamma_2^{-3} \, t_3^{-1}.$$
(8)

Given the hydrodynamic forward-shock evolution in the homogeneous medium $\Gamma \sim 101.2 \left(\frac{1+z}{1.5}\right)^{\frac{3}{8}} E_{53.5}^{\frac{1}{8}} n^{-\frac{1}{8}} t_3^{-\frac{3}{8}}$, and the photon energy radiated by synchrotron $\epsilon_{\gamma}(\gamma_e) \propto \Gamma B' \gamma_e^2$, the synchrotron spectral breaks and the maximum flux evolve as $\epsilon_{\rm m}^{\rm syn} \propto t^{-\frac{3}{2}}$, $\epsilon_{\rm c}^{\rm syn} \propto t^{-\frac{1}{2}}$ and $F_{\rm max}^{\rm syn} \propto t^0$ (e.g., Sari et al. 1998). Taking into consideration the electron Lorentz factors

Taking into consideration the electron Lorentz factors (Equation (8)) and the synchrotron spectral breaks (Sari et al. 1998), the spectral breaks and the maximum flux for SSC emission can be written as

$$\begin{split} \epsilon_{\,\,\mathrm{m}}^{\,\,\mathrm{ssc}} &\simeq 11.4\,\mathrm{keV}g(p)^4 \! \left(\frac{1+z}{1.5} \right)^{\!\!\frac{3}{4}} \varepsilon_{e,-2}^4 \varepsilon_{\mathrm{B},-4}^{\!\!\frac{1}{2}} n^{-\frac{1}{4}} E_{53.5}^{\!\!\frac{3}{4}} \, t_3^{-\frac{9}{4}}, \\ \epsilon_{\,\,\mathrm{c}}^{\,\,\,\mathrm{ssc}} &\simeq 0.1\,\,\mathrm{TeV} \! \left(\frac{1+z}{1.5} \right)^{\!\!-\frac{3}{4}} \! \left(\frac{1+Y_{\mathrm{Th}}}{2.5} \right)^{\!\!-4} \varepsilon_{\mathrm{B},-4}^{-\frac{7}{2}} \, n^{-\frac{9}{4}} \, E_{53.5}^{-\frac{5}{4}}, \\ &\qquad \qquad \times t_3^{-\frac{1}{4}}, \end{split}$$

$$F_{\,\,\mathrm{max}}^{\,\,\,\mathrm{ssc}} &\simeq 1.1 \quad \times \quad 10^{-5}\,\,\mathrm{mJy} \! \left(\frac{1+z}{1.5} \right)^{\!\!\frac{3}{4}} \varepsilon_{\mathrm{B},-4}^{\!\!\frac{1}{2}} \, n^{\frac{5}{4}} \, D_{27}^{-2} \, E_{53.5}^{\,\,\frac{5}{4}} \, t_3^{\,\,\frac{1}{4}}. \end{split}$$

Given the synchrotron spectra for the fast- and slow-cooling regimes together with the SSC spectral breaks and the maximum flux (Equation (9)), the SSC light curves in the fast- (slow)-cooling regimes are (Sari & Esin 2001)

$$\begin{split} F_{\nu}^{\text{ssc}} &= \\ \begin{cases} F_{1,\text{f(s)}}^{\text{H}} t_{3}^{\frac{1}{3}} \left(t_{3} \right) \epsilon_{\gamma,11}^{\frac{1}{3}}, & \epsilon_{\gamma} < \epsilon_{\text{c}}^{\text{ssc}} (\epsilon_{\text{m}}^{\text{ssc}}), \\ F_{2,\text{f(s)}}^{\text{H}} t_{3}^{\frac{1}{8}} \epsilon_{\gamma,11}^{-\frac{1}{2}} \left(t_{3}^{-\frac{9p-11}{8}} \epsilon_{\gamma,11}^{-\frac{p-1}{2}} \right), & \epsilon_{\gamma,c}^{\text{ssc}} (\epsilon_{\text{m}}^{\text{ssc}}) < \epsilon_{\gamma} < \epsilon_{\text{m}}^{\text{ssc}} (\epsilon_{\text{c}}^{\text{ssc}}), \\ F_{3,\text{f(s)}}^{\text{H}} t_{3}^{-\frac{9p-10}{8}} \epsilon_{\gamma,11}^{-\frac{p}{2}}, & \left\{ \epsilon_{\text{c}}^{\text{ssc}}, \epsilon_{\text{m}}^{\text{ssc}} \right\} < \epsilon_{\gamma}, \end{cases} \end{split}$$

$$(10)$$

where $\epsilon_{\gamma,11} = 100 \,\text{GeV}$ and $t_3 = 1000 \,\text{s}$ correspond to the energy band and timescale at which the flux is estimated. It is worth noting that the time evolution of each PL segment of the SSC light curve agrees with those derived in Panaitescu & Kumar (2000) for the fast- and slow-cooling regimes and the PL segments in the slow-cooling regime derived by Sari & Esin (2001).

For the case of the homogeneous medium, the spectral break caused by the decrease of the scattering cross section, due to the KN effect, is given by

$$\epsilon_{c}^{KN} \simeq 0.7 \text{ GeV} \left(\frac{1+z}{1.5}\right)^{-\frac{3}{4}} \left(\frac{1+Y_{Th}}{2.5}\right)^{-1} \varepsilon_{B,-4}^{-1} n^{-\frac{3}{4}} E_{53.5}^{-\frac{1}{4}} \times t_{3}^{-\frac{1}{4}}.$$
(11)

The light curves given in Equation (10) show two important features. (i) They show that at lower energies the SSC flux increases with time and at higher energies it decreases in both

 $[\]overline{8}$ The energy break of scattering photons above which the scatterings with the electron population given by Lorentz factor γ_e lie the KN regime is given by $\epsilon_{\rm KN}^{\rm syn}(\gamma_e)=m_e~c^2\frac{\Gamma}{\gamma_e}$ (Wang et al. 2010; Beniamini et al. 2015). For $\gamma_e=\gamma_c$, Equations (1) and (5) are related by $\epsilon_{\rm KN}^{\rm syn}(\gamma_c)=\frac{\epsilon_{\rm KN}^{\rm syn}}{\gamma_c^2}\simeq 2.1~{\rm keV}$. Taking into account that the electron Lorentz factor of $\gamma_e^*\simeq 3\times 10^7$ produces the synchrotron photons at $\sim\!300~{\rm MeV}$, the corresponding KN photon energy is $\epsilon_{\rm KN}^{\rm syn}(\gamma_e^*)\simeq 1.4~{\rm eV}$. Given that the characteristic and cutoff synchrotron breaks are $\epsilon_{\rm m}^{\rm syn}=1.6~{\rm eV}$ and $\epsilon_c^{\rm syn}=0.2~{\rm keV}$, respectively, the Compton parameter lies in the range $\epsilon_{\rm KN}^{\rm syn}(\gamma_e^*)<\epsilon_{\rm m}^{\rm syn}<\epsilon_c^{\rm syn}<\epsilon_c^{\rm syn}(\gamma_c)$. For this case, $Y(\gamma_e^*)=Y_{\rm Th}\left(\frac{\epsilon_{\rm m}^{\rm syn}}{\epsilon_c^{\rm syn}}\right)^{\frac{3}{2}}\left(\frac{\epsilon_{\rm KN}(\gamma_e^*)}{\epsilon_{\rm m}^{\rm syn}}\right)^{\frac{4}{3}}\simeq 0.57~Y_{\rm Th}$ with $Y_{\rm Th}=1.93$.

 $^{^{9}}$ This relation was obtained using the synchrotron and SSC luminosity ratio derived in Sari & Esin (2001) with the equivalent density for the stratified medium.

regimes (fast and slow). This indicates that SSC emission is more likely to be detected during the first seconds after the trigger time, although if this emission is very strong it can be observed for long times. It is worth highlighting that the SSC emission at lower energies is eclipsed by the synchrotron radiation. (ii) The first PL segment in the fast-cooling regime $(\epsilon_{\gamma} < \epsilon_{\rm c}^{\rm ssc})$, and the third PL segments $(\{\epsilon_{\rm c}^{\rm ssc}, \epsilon_{\rm m}^{\rm ssc}\} < \epsilon_{\gamma})$ are decaying functions of the circumburst density. This suggests that, depending on the timescale and energy range observed, the SSC emission could be detected in environments with higher and/or lower densities.

The bottom panels in Figure 1 show the resulting light curves and SEDs of the SSC forward-shock emission generated by a decelerating outflow in a homogeneous medium. These panels were obtained using relevant values for GRB afterglows. 10 The observable quantities, the microphysical parameters, the circumburst density, and the efficiencies for a homogeneous density are in the range proposed to produce GeV photons in the afterglow phase (e.g., see Beniamini et al. 2015, 2016). Again, the effect of the EBL absorption proposed by Franceschini & Rodighiero (2017) was considered. The bottom left-hand panel shows that the SSC flux is above the Fermi-LAT and MAGIC sensitivities during the first $100 \, s$ for n = $0.1 \,\mathrm{cm}^{-3}$ but not for the value of $n = 10^{-3} \,\mathrm{cm}^{-3}$. The gold and blue solid curves in the top left-hand panel correspond to 10 and 100 GeV, respectively, and the gold and blue dasheddotted curves to the Fermi-LAT (Piron 2016) and the MAGIC (Takahashi et al. 2008) sensitivities at the same energies, respectively. The purple and green curves in the right-hand panel correspond to the SEDs at 10 and 100 s, respectively.

The bottom panels of Figure 1 show that the SSC flux is very sensitive to the external density. The light curves above the Fermi-LAT and MAGIC sensitivities are obtained with $n = 10^{-1} \,\mathrm{cm}^{-3}$ and below with $n = 10^{-3}$ cm⁻³. In this particular case, both light curves (at 10 and 100 GeV) evolve in the second PL segment of the slow-cooling regime. The spectral breaks are $\epsilon_{\rm m}^{\rm ssc}=36.1~{\rm keV}$ and $\epsilon_{\rm c}^{\rm ssc}=5.3\times10^3~{\rm TeV}~{\rm for}~n=10^{-3}~{\rm cm}^{-3},$ and $\epsilon_{\rm m}^{\rm ssc}=11.4~{\rm keV}$ and $\epsilon_{\rm c}^{\rm ssc}=0.2~{\rm TeV}~{\rm for}~n=0.1~{\rm cm}^{-3},$ respectively. The transition times between the fast- to slow-cooling regimes are 0.06 s and 0.6 s for $n = 10^{-3}$ cm⁻³ and 0.1 cm⁻³, respectively. This shows that, with the chosen values, the SSC emission decreases monotonically with time and increases as the density of the circumburst medium increases. Using the parameter values, the break energies in the KN regime are 31.7 TeV and 1.1 TeV for $n = 10^{-3}$ and $0.1 \,\mathrm{cm}^{-3}$, respectively, which are above the energies of the Fermi-LAT and MAGIC sensitivities. Again, we emphasize that, depending on the parameter values, the SSC emission would lie in the KN regime, and then this will be drastically suppressed. Similarly, the electron population that upscatters synchrotron photons beyond the KN regime would be altered (Nakar et al. 2009; Wang et al. 2010).

The bottom left-hand panel of Figure 1 shows that the SSC flux at 10 GeV is above the *Fermi*-LAT sensitivity after \sim 30 s and at 100 GeV is above MAGIC sensitivity during the first 850 s for $n=0.1~\rm cm^{-3}$ but not for $n=10^{-3}~\rm cm^{-3}$. Therefore, the probability to detect the SSC emission from the GRB afterglow depends on the observed energy. For $\epsilon_{\gamma}=10~\rm GeV$, the SSC emission could be detected delayed with respect to the

prompt phase whereas for $\epsilon_{\gamma} = 100 \text{ GeV}$ it could be detected in temporal coincidence with lower-energy photons.

The bottom right-hand panel of Figure 1 shows the SEDs for the same parameter densities at $t=10^3$ s and 10^4 s. The value of n=0.1 cm⁻³ corresponds to the curve above the *Fermi-LAT* and MAGIC sensitivities and the value of $n=10^{-3}$ cm⁻³ to the curve below these sensitivities. The red dashed line corresponds to the maximum energy radiated by synchrotron. The filled areas in gray and cyan colors correspond to the *Fermi-LAT* and MAGIC energy ranges, respectively. The *Fermi-LAT* and MAGIC areas show that photons above the synchrotron limit can be explained by SSC emission, similar to the case of the stratified medium. The maximum SSC flux, due to EBL absorption, lies at the lower end of the MAGIC energy range, making this telescope ideal for detecting the SSC emission generated in a homogenous medium.

In order to compare the synchrotron and SSC fluxes at *Fermi*-LAT energies (e.g., $\epsilon_{\gamma} = 800$ MeV), we obtain the synchrotron and SSC spectral breaks at $t = 10^3$ s for n = 0.1 cm⁻³ ($\epsilon_{\rm m}^{\rm syn} = 6.1 \times 10^{-2}$ eV, $\epsilon_{\rm c}^{\rm syn} = 0.3$ keV $\epsilon_{\rm m}^{\rm ssc} = 11.4$ keV $\epsilon_{\rm c}^{\rm ssc} = 0.2$ TeV). Therefore, at the *Fermi*-LAT energy range the synchrotron emission evolves in the third PL segment of the slow-cooling regime and the SSC emission in the second PL segment. In this case, the ratio of synchrotron and SSC fluxes becomes

$$\frac{F_{\nu}^{\text{syn}}}{F_{\nu}^{\text{ssc}}} \sim 1.9 \left(\frac{1+z}{1.5}\right)^{-\frac{1}{4}} \left(\frac{1+Y_{\text{Th}}}{1.4}\right)^{-1} \varepsilon_{e,-2}^{1-p} \varepsilon_{\text{B},-4}^{-\frac{3}{4}} n_{-1}^{-\frac{7}{6}} E_{53.5}^{-\frac{1}{12}}
\Gamma_{2.5}^{\frac{5}{3}-p} t_{2}^{-\frac{1}{4}} \left(\frac{\epsilon_{\gamma}}{800 \text{ MeV}}\right)^{-\frac{1}{2}},$$
(12)

which is of order unity. We want to emphasize that the synchrotron and SSC flux ratio depends explicitly on *Y*. For the homogeneous medium, we use a smaller value of the effective Compton *Y* parameter because electrons radiating synchrotron at these large energies have a Compton *Y* parameter smaller than the corresponding value in the Thomson regime. We can conclude that below ~400 MeV the observations can be described in the synchrotron forward-shock scenario, between ~0.6 and 1 GeV the contribution of both processes would be relevant, and beyond the synchrotron limit, the observations would be entirely explained by SSC process for the set of values used.

The bottom right-hand panel of Figure 1 shows that the maximum SSC flux lies at $\sim 100\,\mathrm{GeV}$, making it possible to detect the VHE emission in observatories where the sensitivity is maximum at hundreds of GeV but not in those observatories where the maximum sensitivity lies at a few TeV (e.g., HAWC; Abeysekara et al. 2012). Similar to the case of the stratified medium, the SSC flux at 1 TeV decreases between two and three orders of magnitude in comparison with the flux at $100\,\mathrm{GeV}$.

 $[\]overline{{}^{10}}~E=5\times 10^{53}~{\rm erg},~p=2.3,~\varepsilon_{\rm B}=10^{-3},~\varepsilon_e=10^{-2},~z=0.5~{\rm and}~n=10^{-3}~(10^{-1})~{\rm cm}^{-3}~{\rm for~the~purple~(green)~curve}.$

¹¹ For the homogeneous medium, an analysis of the effective Y parameter for electrons radiating synchrotron at Fermi-LAT energies can also be done. In this case, the break energies are $\epsilon_{\rm KN}(\gamma_{\rm c})=\frac{\epsilon_{\rm KN}^{\rm e}}{\gamma_{\rm c}^2}\simeq 0.9~{\rm keV}, \epsilon_{\rm KN}(\gamma_{\rm e}^*)\simeq 0.6~{\rm eV},$ $\epsilon_{\rm m}^{\rm syn}=0.7~{\rm eV}$ and $\epsilon_{\rm c}^{\rm syn}=0.1~{\rm keV}.$ Again, the Compton parameter corresponding to the case $\epsilon_{\rm KN}(\gamma_{\rm e}^*)<\epsilon_{\rm m}^{\rm syn}<\epsilon_{\rm c}^{\rm syn}<\epsilon_{\rm KN}(\gamma_{\rm c})$ is $Y(\gamma_{\rm e}^*)\simeq 0.28~Y_{\rm Th}$ with $Y_{\rm Th}=1.45.$ Therefore, a similar conclusion to that found in the stratified case is given.

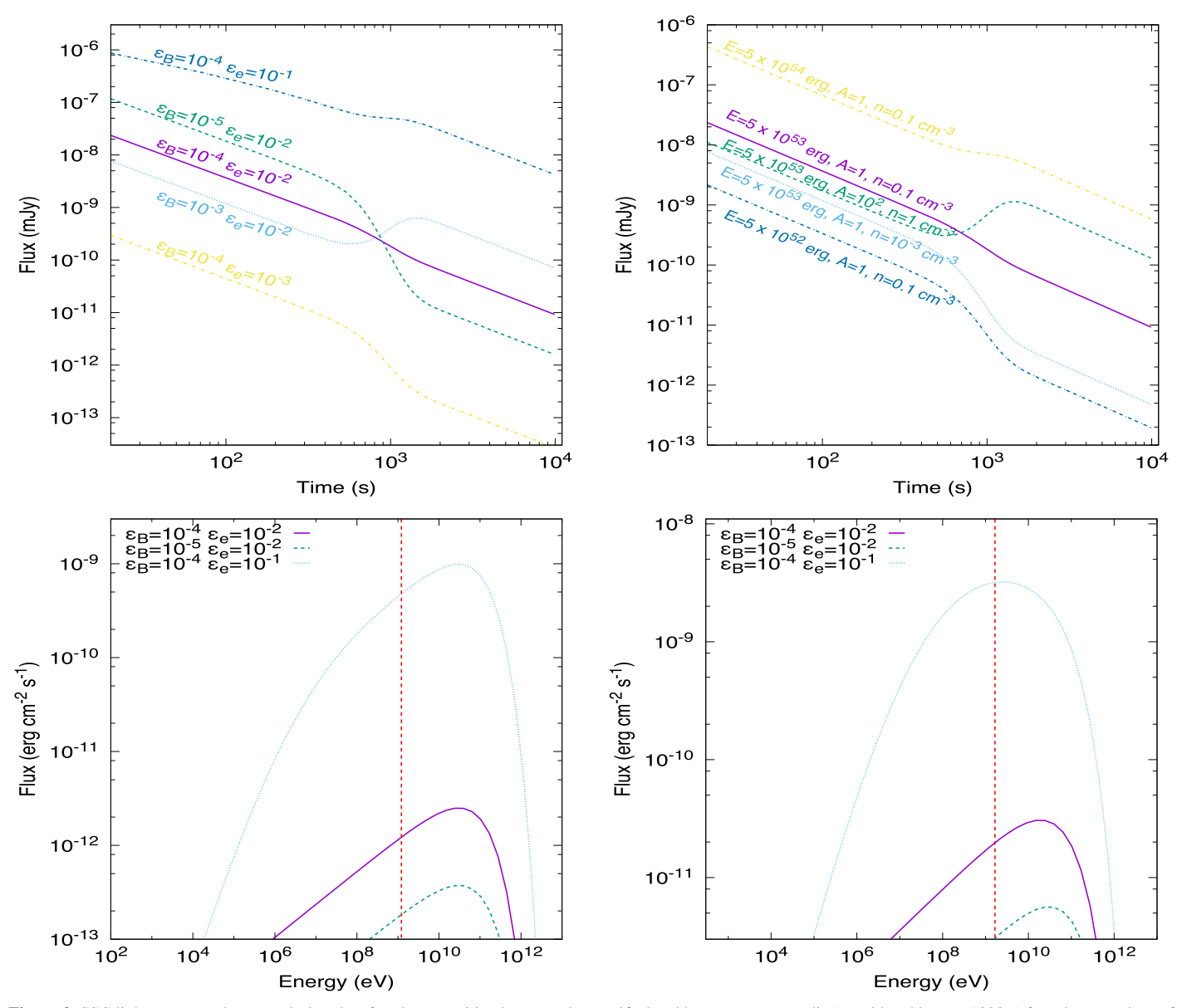


Figure 2. SSC light curves and spectra during the afterglow transition between the stratified and homogeneous media (considered here at 1000 s) for relevant values of GRB afterglows. In the top left-hand panel, light curves are obtained for $E=5\times10^{53}$ erg, $A_{\rm w}=1$, and n=1 cm⁻³, and in the top right-hand panel these are for $\varepsilon_{\rm B}=10^{-4}$ and $\varepsilon_{\rm B}=10^{-2}$. The top panels show the SSC light curves for $\epsilon_{\gamma}=100$ GeV and the bottom ones the SSC spectra computed in the stratified (left) and homogeneous (right) medium. The SSC spectra in the stratified medium are computed for t=900 s and in the homogeneous medium for t=1100 s. The red dashed line corresponds to the maximum energy radiated by synchrotron.

Given the minimum and cooling electron Lorentz factors (Equation (8)), the synchrotron and SSC luminosity ratio can be computed as (Sari & Esin 2001)

$$\frac{L_{\nu}^{\text{ssc}}}{L_{\nu}^{\text{syn}}} \simeq 5.1 \times 10^{-2} \, n_{-1} \, R_{\text{dec},17} \, \gamma_{\text{c},4}^2 \left(\frac{\gamma_{\text{c},4}}{\gamma_{\text{m},2}} \right)^{1-p}, \tag{13}$$

where $R_{\rm dec}=4.22\times 10^{17}\,{\rm cm}\left(\frac{1+z}{1.5}\right)^{-\frac{1}{4}}n_{-1}^{-\frac{1}{4}}\,E_{53.5}^{\frac{1}{4}}\,t_3^{\frac{1}{4}}$ is the deceleration radius. Again, it is worth mentioning that the synchrotron and SSC luminosity ratio depends on Y through γ_c . In the case of the uniform medium, only 5% of the synchrotron luminosity is up-scattered by SSC emission.

2.3. The Stratified-to-homogeneous Afterglow Transition

Figure 2 shows the SSC light curves and spectra during the afterglow transition between the stratified and homogeneous media for typical values in the ranges $5\times 10^{52}\leqslant E\leqslant 5\times 10^{54}~\rm erg,~0.1~cm^{-3}\leqslant n\leqslant 1~cm^{-3},~10^{-2}\leqslant A_{\rm w}\leqslant 1,~10^{-5}\leqslant \varepsilon_{\rm B}\leqslant 10^{-3},~\rm and~10^{-3}\leqslant \varepsilon_{\rm e}\leqslant 10^{-1}.$ The top panels show the SSC light curves for $\epsilon_{\gamma}=100~\rm GeV.$ The stratified-to-homogeneous transition radius can be written as (e.g., see Fraija et al. 2017b)

$$R_{\rm tr} \simeq 5.1 \times 10^{18} \,{\rm cm}\,\dot{M}_{-0}^{\frac{3}{10}} \,v_{\rm W,8}^{\frac{1}{10}} \,n^{-\frac{3}{10}} \,t_{\star,5}^{\frac{2}{5}},$$
 (14)

where t_{\star} is the lifetime of the star phase for $n = 1 \text{ cm}^{-3}$. In our analysis, we have considered the stratified-to-homogeneous

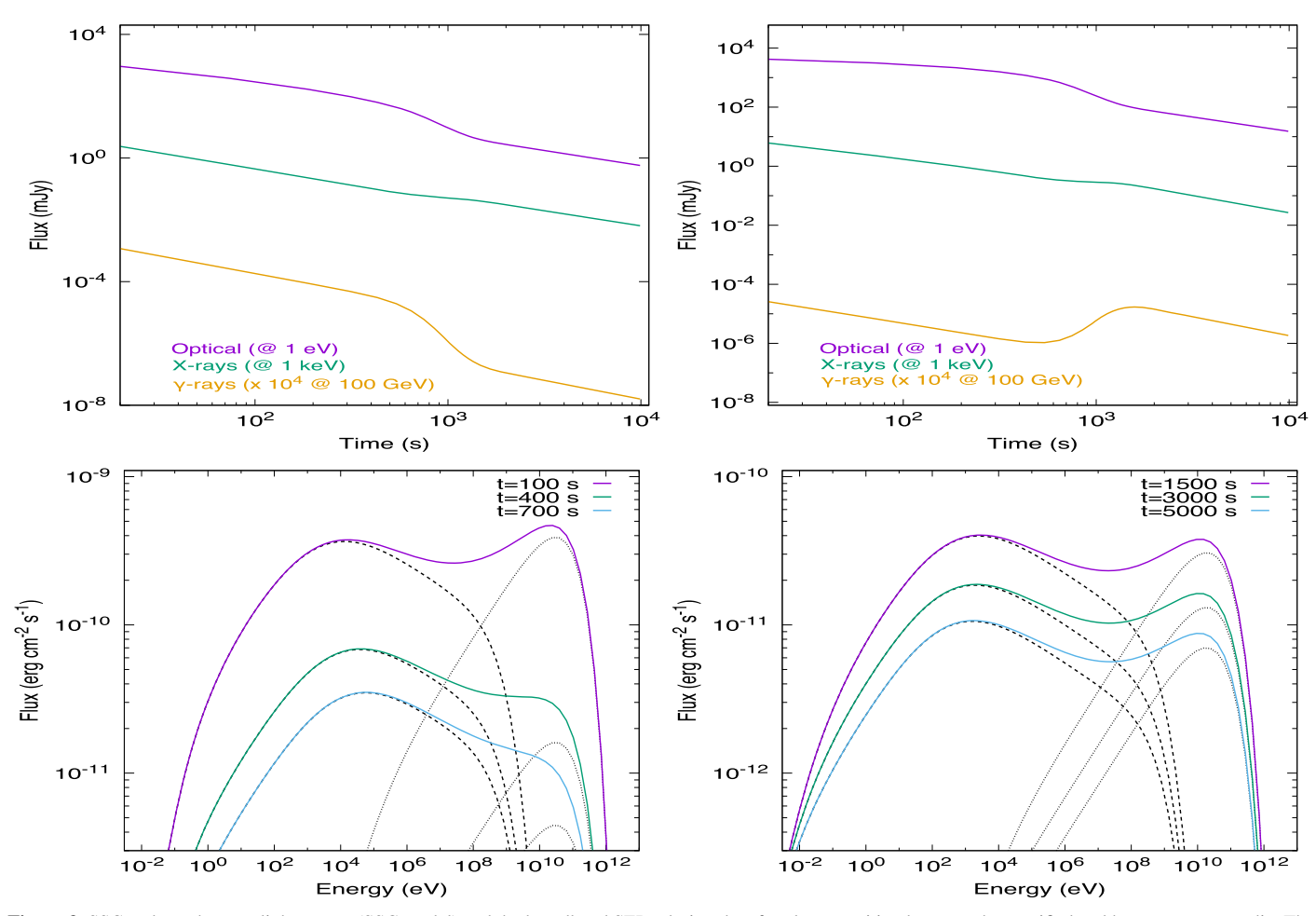


Figure 3. SSC and synchrotron light curves (SSC model) and the broadband SEDs during the afterglow transition between the stratified and homogeneous media. The top panels show the synchrotron light curves of optical and X-ray bands at 1 eV and 1 keV, and the SSC light curves of γ -rays at 100 GeV. In the top left-hand panel, the light curves are computed for $E=5\times10^{53}$ erg, $A_{\rm w}=0.1$, n=0.1 cm⁻³, $\varepsilon_{\rm B}=10^{-4}$, $\varepsilon_{\rm e}=10^{-2}$, and $\xi=1$, and in the top right-hand panel, these are obtained for $E=10^{54}$ erg, $A_{\rm w}=1$, n=1 cm⁻³, $\varepsilon_{\rm B}=10^{-3}$, $\varepsilon_{\rm e}=10^{-2}$, and $\xi=0.5$. The bottom panels show the broadband SEDs (both synchrotron—dashed and SSC—dotted) computed in the stratified medium for t=100, 400, and 700 s (left) and the homogeneous medium for t=1500, 3000, and 5000 s (right). The stratified-to-homogeneous transition is considered at 1000 s, as in Figure 2. In the bottom panels, the SEDs are computed for $E=5\times10^{53}$ erg, $\varepsilon_{\rm B}=10^{-4}$, and $\varepsilon_{\rm e}=10^{-2}$, with the densities of $A_{\rm W}=0.1$ (left) and n=1 cm⁻³ (right).

afterglow transition at 1000 s which corresponds to a deceleration radius of $\simeq 4.2 \times 10^{18}$ cm for $E=5 \times 10^{54}$ erg and $A_{\rm W}=10^{-1}$ or $E=5 \times 10^{53}$ erg and $A_{\rm W}=10^{-2}$. In the top left-hand panel, the light curves are computed for $E=5 \times 10^{53}$ erg, $A_{\rm w}=1$, and $n = 1 \text{ cm}^{-3}$ and in the top right-hand panel the light curves are obtained for $\varepsilon_{\rm B}=10^{-4}$ and $\varepsilon_{e}=10^{-2}$. These panels show that, depending on the parameter values, the afterglow transition can be quite noticeable. For instance, in the purple curve there is actually a smoother transition (which is harder to detect) compared to some of the others. The top left-hand panel shows that SSC fluxes increase as ε_e increases in the stratified and the homogeneous medium; higher values of ε_e make SSC emission more favorable to be detected (indeed such values are expected to be common in GRB afterglows; see e.g., Santana et al. 2014; Beniamini & van der Horst 2017). Moreover, the SSC fluxes increase as $\varepsilon_{\rm B}$ decreases in the stratified but not in the homogeneous medium. The top right-hand panel shows that the SSC fluxes increase as E, n, and AW increase in both the stratified and homogeneous media.

The bottom panels of Figure 2 show the SSC spectra computed in the stratified medium for $t=900\,\mathrm{s}$ (left panel) and in the homogeneous medium for $t=1100\,\mathrm{s}$ (right panel). The red dashed line represents the synchrotron limit. The bottom panels show that these spectra increase dramatically as ϵ_{e} increases and slightly as ϵ_{B} increases. The SSC light curves with the same colors (parameter values) represent the evolution from the stratified to the homogeneous medium. As a consequence of this transition, one can observe that SSC fluxes increase up to more than one order of magnitude.

Figure 3 shows the synchrotron and SSC light curves and the SEDs during the afterglow transition between the stratified and homogeneous media. The spectrum and light curves of synchrotron emission have been included with the purpose of performing a multi-wavelength analysis.

2.3.1. Multi-wavelength Light Curve Analysis

The synchrotron light curves of optical and X-ray bands at 1 eV and 1 keV, and the SSC light curves of γ -rays at 100 GeV, are shown in the top panels of Figure 3. In both panels it can be seen

that, while optical and X-ray fluxes display the same behavior, γ -rays exhibit a different one. For the given parameter values, during the afterglow transition the γ -ray flux can decrease (left panel) or increase (right panel). Taking into consideration the parameter values used in the top left-hand panel, for the stratified medium the synchrotron and the SSC spectral breaks are $\epsilon_{\rm m}^{\rm syn}=5.1\times 10^{-2}~{\rm eV},~\epsilon_{\rm c}^{\rm syn}=2.3~{\rm keV},~\epsilon_{\rm m}^{\rm ssc}=15.1~{\rm keV},~\epsilon_{\rm c}^{\rm ssc}=97.7~{\rm TeV},~\epsilon_{\rm c}^{\rm KN}=8.8~{\rm TeV},~{\rm and}~{\rm for}~{\rm the~homogeneous~medium}$ these breaks are $\epsilon_{\rm m}^{\rm syn}=2.2\times 10^{-2}~{\rm eV},~\epsilon_{\rm c}^{\rm syn}=1.8~{\rm keV},~\epsilon_{\rm m}^{\rm ssc}=3.6~{\rm keV},~\epsilon_{\rm c}^{\rm ssc}=8.3~{\rm TeV},~\epsilon_{\rm c}^{\rm KN}=2.4~{\rm TeV}.$ Considering the parameter values used in the right-hand panel, the SSC and synchrotron spectral breaks computed in the stratified medium are synchrotron spectral breaks computed in the stratified medium are $\epsilon_{\rm m}^{\rm syn}=4.3~{\rm eV},~\epsilon_{\rm c}^{\rm syn}=3.5\times10^{-2}~{\rm eV},~\epsilon_{\rm m}^{\rm ssc}=0.5~{\rm MeV},~\epsilon_{\rm c}^{\rm ssc}=0.5~{\rm keV},~\epsilon_{\rm c}^{\rm syn}=4.9~{\rm GeV}$ and these breaks computed in the homogeneous medium are $\epsilon_{\rm m}^{\rm syn}=8.5\times10^{-2}~{\rm eV},~\epsilon_{\rm c}^{\rm syn}=14.3~{\rm eV},~\epsilon_{\rm m}^{\rm ssc}=10.8~{\rm keV},~\epsilon_{\rm c}^{\rm ssc}=0.2~{\rm GeV},~\epsilon_{\rm c}^{\rm KN}=2.6~{\rm GeV}.$ Therefore, from the stratified to homogeneous media the optical flux constants in the second BL constants and the X-ray in the flux evolves in the second PL segment and the X-rays in the third PL segment of synchrotron model. During this transition phase the temporal index of the third PL segment of synchrotron emission $(\propto t^{-\frac{3p-2}{4}})$ does not vary, and the second PL segment varies from $\propto t^{-\frac{3p-1}{4}}$ to $\propto t^{-\frac{3p-3}{4}}$. However, an alternative interpretation different from the afterglow transition could be given in terms of the reverse-shock emission. In this framework, the X-rays are not altered and the optical flash is detected with a decay flux $\propto t^{-\frac{73p+21}{96}}$ and $\propto t^{-\frac{27p+7}{35}}$ for the thick and thin shell, respectively (Kobayashi 2000). In this case, the analysis of the SSC light curve would be very useful in order to differentiate both interpretations. With the given parameters, the γ -ray evolves in the second PL segment close to the afterglow transition, from $\propto t^{-p}$ to $\propto t^{-\frac{1}{8}}$. With these parameters, the γ -ray evolves in the second PL segment as the medium changes from wind to ISM from $\propto t^{-p}$ or $\propto t^{-\frac{1}{8}}$, respectively; if the medium did not have this transition, then the flux would not show this particular break in the light curve. It is worth noting that, while the afterglow transition is imperceptible for the synchrotron light curve at 1 keV, it presents a discontinuity quite evident for the SSC light curve at 100 GeV.

2.3.2. The Broadband SED Analysis

The bottom panels of Figure 3 show the SEDs computed in the stratified (left panel) and homogeneous (right panel) medium for a transition at 1000 s. For the stratified medium, we assume each SED at 100, 400, and 700 s and, for the homogeneous medium, we calculate each SED at 1500, 3000, and 5000 s. Densities with values of A = 0.1 and n = 1 cm⁻³ are chosen for the stratified and homogeneous media, respectively, and in both cases we use the same values $E=5\times10^{53}\,\mathrm{erg},\,\varepsilon_{\mathrm{B}}=10^{-4},\,\mathrm{and}\,\varepsilon_{e}=10^{-2}$ and $\xi = 1.0$. The principal features are: (i) while the ratio between the maximum synchrotron and the SSC fluxes decreases drastically in the stratified medium, it remains quasi-constant in the homogeneous medium; (ii) while the synchrotron peak is shifted to higher energies as time increases in the stratified medium, it evolves quite slowly with time in the homogeneous medium; (iii) while the maximum value of the SSC flux decreases rapidly with time for the stratified medium, this value decreases gradually for the homogeneous medium; (iv) an increase in the synchrotron and SSC fluxes is seen during the afterglow transition; at $t = 700 \,\mathrm{s}$ the maximum values of synchrotron and SSC fluxes are 3.5×10^{-11} and 4.2×10^{-12} erg cm⁻² s⁻¹, respectively, and at t = 1500 s the maximum values of synchrotron and SSC fluxes are 4.2×10^{-11} and 3.1×10^{-11} erg cm⁻² s⁻¹; (v) the evolution of the SED structures in both the stratified and homogeneous media are different. These characteristics could help identify if the transition phase exists or is simply associated with a distinct scenario.

3. Application to GRB 190114C

3.1. Multi-wavelength Observations and Previous Analysis

GRB 190114C was triggered by the BAT instrument onboard the *Swift* satellite on 2019 January 14 at 20:57:06.012 UTC (Gropp et al. 2019). VHE photons with energies above 300 GeV were detected from this burst with a significance of 20σ by the MAGIC telescope for more than 20 min (Mirzoyan et al. 2019). GRB 190114C was followed up by a massive observational campaign with instruments onboard satellites and ground telescopes covering a large fraction of the electromagnetic spectrum (see Fraija et al. 2019c and references therein). The host galaxy of GRB 190114C was located and confirmed to have a redshift of z=0.42 (Selsing et al. 2019; de Ugarte Postigo et al. 2019).

Recently, Fraija et al. (2019c) showed that the LAT light curve of GRB 190114C exhibited similar features to other bright LAT-detected bursts. Together with the multi-wavelength observations, the long-lived LAT, GBM, X-ray, optical, and radio emissions were consistent with the standard synchrotron forward-shock model that evolves from a stratified to a homogeneous medium with an afterglow transition at ~400 s. These authors showed that the high-energy photons were produced in the deceleration phase of the relativistic outflow and also that some additional processes to synchrotron in the forward shocks should be considered to properly describe the LAT photons with energies beyond the synchrotron limit. Here, we use the SSC process to interpret the photons beyond this synchrotron limit.

3.2. Estimation of SSC Light Curves and VHE Photons beyond the Synchrotron Limit

Using the best-fit values reported in Fraija et al. (2019c), the SSC light curves were calculated. The left-hand panel in Figure 4 shows the SSC light curves at 100 GeV in a stratified and a homogeneous medium. This panel was adapted from Fraija et al. (2019c). The effect of the EBL absorption proposed by Franceschini & Rodighiero (2017) was included.

The values of transition times between the fast- and slowcooling regimes are 0.2 s and 0.09 s for the stratified and homogenous medium, respectively. The values of the characteristic and cutoff SSC breaks calculated in the stratified medium are $\epsilon_{\rm m}^{\rm ssc}\simeq 0.2~{\rm MeV}$ and $\epsilon_{\rm c}^{\rm ssc}\simeq 4.2~\times 10^4~{\rm keV}$ at $100~{\rm s}$, and in the homogeneous medium are $\epsilon_{\rm m}^{\rm ssc}\simeq 1.6~{\rm keV}$ and $\epsilon_{\rm c}^{\rm ssc} \simeq 1.6$ keV, respectively, at 1000 s. Therefore, in both cases the SSC light curves evolve in the second PL segment of the slow-cooling regime. The break energies in the KN regime are 200.7 TeV and 868.1 GeV at 100 s and 10³ s, respectively. The highest-energy photons reported by Fermi-LAT and MAGIC collaboration are below the KN regime, which agrees with the description of the SSC light curves. We emphasize that the parameters obtained with the MCMC code from the broadband modeling of the multi-wavelength observations may be changed somewhat when the KN effects are included, but the SSC emission itself will not be strongly affected. Therefore,

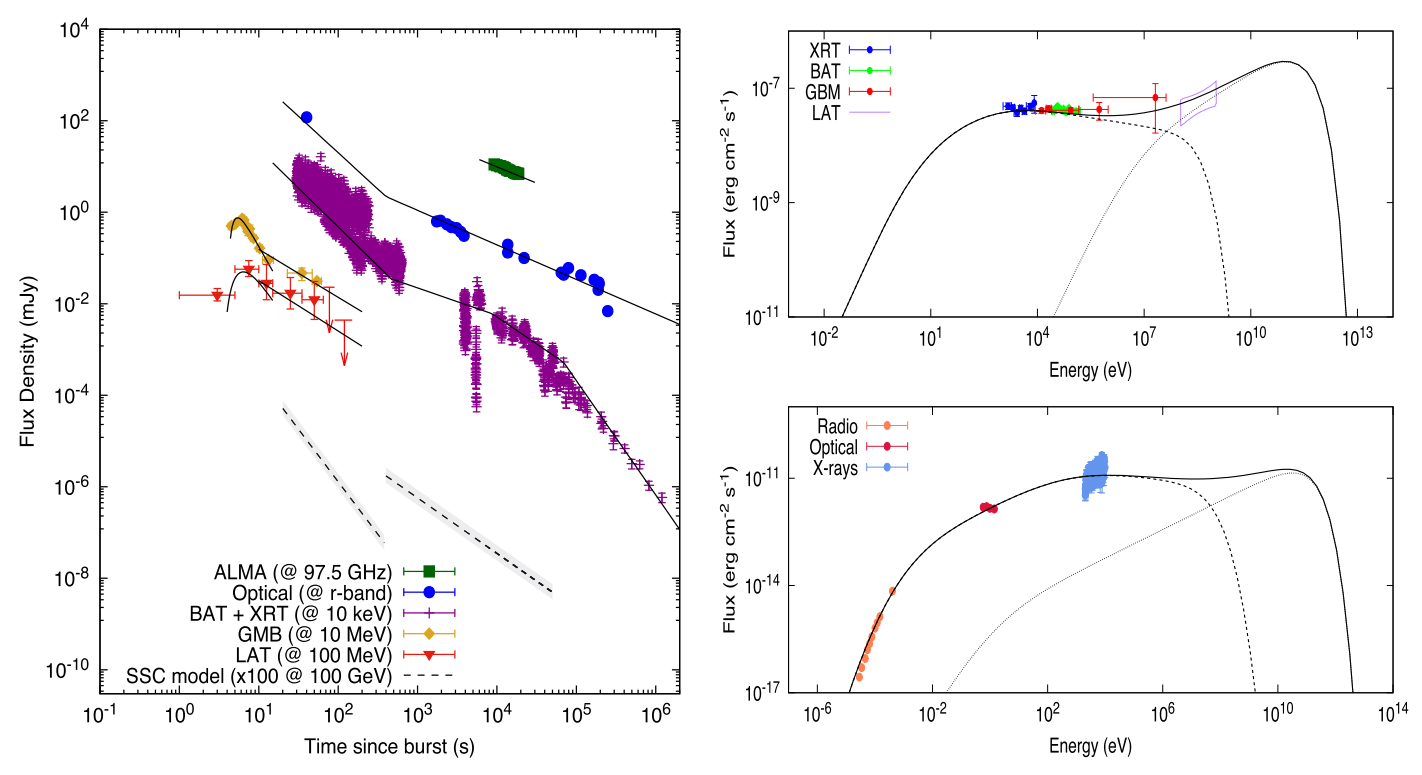


Figure 4. SSC light curves (left) and SEDs (right) of GRB 190114C. The synchrotron and SSC curves in a stratified and a homogeneous medium are derived using the best-fit parameters reported in Fraija et al. (2019c). The broadband SEDs are built from two time intervals 66–92 s (above) and 0.2 day (below). The left-hand panel is adapted from Fraija et al. (2019c). The effect of the extragalactic background light absorption proposed by Franceschini & Rodighiero (2017) is taken into account. Radio, optical, X-ray, GBM, and LAT data are taken from Laskar et al. (2019), Fraija et al. (2019c), and Ravasio et al. (2019). The values used to obtain the SSC light curves and SEDs are $A_W = 6 \times 10^{-2}$, n = 1 cm⁻³, $E = 2 \times 10^{54}$ erg, $\varepsilon_B = 5 \times 10^{-6}$, $\varepsilon_e = 10^{-2}$, and p = 2.3 (Fraija et al. 2019c).

VHE photons beyond the synchrotron limit can be explained through the second PL segment of the SSC emission in the slow-cooling regime.

In our model, the SSC emission decays more steeply in the stratified than in the homogeneous medium. However, during the stratified-to-homogeneous transition the SSC flux suddenly increases by around one order of magnitude. This allows that the SSC component could be detected over a longer time.

Abeysekara et al. (2012) applied the HAWC sensitivity of the scaler system to GRBs for several declinations and energies (at which this observatory is sensitive). At 1 TeV and for a power-law index of $p=2.15\pm0.35$, the HAWC sensitivities for the declinations of $1.0 \ge \cos\theta > 0.9$, $0.9 \ge \cos\theta > 0.8$, $0.8 \ge \cos\theta > 0.7$, and $0.7 \ge \cos\theta > 0.6$ are $\sim (2.2 \times 10^{-7} - 1.1 \times 10^{-6})$ mJy, $\sim (0.4 \times 10^{-6} - 2.5 \times 10^{-6})$ mJy, $\sim (0.8 \times 10^{-6} - 0.7 \times 10^{-5})$ mJy, and $\sim (0.8 \times 10^{-5} - 0.7 \times 10^{-4})$ mJy, respectively. Taking into account the attenuation factor $\sim 10^{-2}$ due to EBL at 1 TeV, the SSC flux would be $\sim 10^{-10}$ mJy at 10^2 s and $\sim 10^{-12}$ mJy at 10^3 s for the stratified and homogeneous medium, respectively. These values are well below the HAWC sensitivity for any decl. It shows that, with our model, GRB 190114C could not be detected by the HAWC observatory even if this burst had been located at the HAWC's field of view.

Funk et al. (2013) and Piron (2016) applied and discussed the sensitivity to transient sources as a function of duration of the High Energy Stereoscopic System (HESS) CT5 and Cerenkov Telescope Array (CTA) telescopes for distinct energy thresholds. At 500 s, the HESS CT5 and CTA sensitivities for energy

thresholds of 75 and 80 GeV are $\sim 2 \times 10^{-10}$ mJy and $\sim 7 \times 10^{-10}$ mJy, respectively. Therefore, if GRB 190114C had been quickly located by HESS CT5, this burst would have been detected by HESS in accordance with our model. Similarly, bursts with similar features of GRB 190114C are perfect candidates for detection with future VHE facilities (e.g., CTA; Funk et al. 2013).

3.3. The Broadband SEDs

The right-hand panels of Figure 4 show the SEDs at 66–92 s (top panel) and 0.2 day (bottom panel). The synchrotron and SSC curves in a stratified (above) and homogeneous (below) medium were derived using the best-fit parameters reported in Fraija et al. (2019c). The EBL model introduced in Franceschini & Rodighiero (2017) was used. Radio, optical, X-ray, GBM, and LAT data were taken from Laskar et al. (2019), Fraija et al. (2019c), and Ravasio et al. (2019).

The top panel shows that synchrotron emission describes the optical-to-LAT energy range and SSC emission contributes significantly to the LAT observations. The bottom panel shows that synchrotron emission explains the ratio to X-ray data points. The flux ratio at the peaks are $F_{\nu}^{\rm syn}/F_{\nu}^{\rm ssc} \simeq 10$ and $\simeq 1$ at 66–90 s and 0.2 day, respectively. The SEDs can be explained through the evolution of synchrotron and SSC emissions in the stratified and homogeneous media. The decay of SSC emission is steeper than synchrotron radiation; in the stratified medium the decay of SSC and synchrotron evolve as

 $\propto t^{-2.30}$ and $\propto t^{-1.47}$, respectively, and in the homogeneous medium as $\propto t^{-1.21}$ and $t^{-0.97}$, respectively.

3.4. Why GRB 190114C is Special in Comparison to Other LAT-detected Bursts

The VHE flux above ~ 100 GeV begins to be attenuated by pair production with EBL photons (Gould & Schréder 1966). The SSC flux observed is attenuated by $\exp[-\tau_{\gamma\gamma}(z)]$ with $\tau_{\gamma\gamma}(z)$ the photon–photon opacity as a function of redshift. Using the values of the opacities reported in Franceschini & Rodighiero (2017), VHE emission with photons at 300 GeV (1 TeV) is attenuated by 0.15 (2.1 × 10⁻³) and 6.6 × 10⁻³ (2.2 × 10⁻⁶) for z=0.5 and 1, respectively. In the particular case of GRB 190114C, a low redshift of z=0.42 allowed the detection by an Imaging Atmospheric Cerenkov Telescope (IACT) such as MAGIC.

We show that changes in density of the circumburst medium leads to an increase in the SSC emission. The afterglow transition reported in GRB 190114C allowed for enhanced VHE emission increase and hence was detected for a longer period.

The set of the best-fit parameters as reported for GRB 190114C made more favorable its detection by the MAGIC telescopes. We enumerate each one as follows.

- 1. The SSC emission peaked below the KN regime, otherwise it would be drastically attenuated.
- 2. The peak of the SSC emission was reproduced at hundreds of GeV, where MAGIC is more sensitive and the attenuation by EBL is small. Other configurations of parameters lead to peaks at a few TeV where the EBL absorption is much higher and therefore more difficult to detect by by IACTs.
- 3. With the parameters given, the SSC flux evolved in the second PL segment of the slow-cooling regime. In this case, we show that the SSC flux increases as the densities in both the stratified and homogeneous media increase. The values of densities in both cases make the detection of VHE flux more favorable.
- 4. The LAT light curve of GRB 190114C exhibited similar characteristics to other powerful bursts detected by *Fermi*-LAT (see Fraija et al. 2019c). These authors showed that GRB 190114C corresponded to one of the more powerful bursts during the first hundreds of seconds (early afterglow). In this work we show that higher values of the equivalent kinetic energy make the SSC emission more favorable to be detected. Therefore, the total energy reported of this burst favored its detection.

Notwithstanding attempts to detect the VHE emission at hundreds of GeV by IACTs have been an arduous task because the time needed to locate the burst is longer than the duration of the prompt and early-afterglow emission, one detection has been reported (GRB 190114C; Mirzoyan et al. 2019). Over the last two decades, only upper VHE limits have been derived by these telescopes (e.g., see Albert et al. 2007; Aharonian et al. 2009a, 2009b; Acciari et al. 2011; Aleksić et al. 2014; H.E.S.S. Collaboration et al. 2014; Bartoli et al. 2017; Abeysekara et al. 2018). We conclude that the conditions to locate promptly the

early afterglow of GRB 190114C by the MAGIC telescope together with the low-redshift and favorable set of parameters made its detection possible. We want to highlight that no other LAT-detected burst complies with all the requirements mentioned above. It is worth noting that, although GRB 130427A was closer and more energetic than GRB 190114C (Ackermann et al. 2014), it was not located rapidly enough to catch the early afterglow by IACTs. ¹³

4. Conclusions

We have computed the SSC light curves for a stratified stellar wind that transitions to a homogeneous ISM-like medium, taking into account the synchrotron forward-shock models introduced in Sari et al. (1998), Chevalier & Li (2000), and Panaitescu & Kumar (2000). The break energy in the KN regime was obtained. The attenuation produced by the EBL absorption was introduced in accordance with the model presented in Franceschini & Rodighiero (2017). The intrinsic attenuation by e^{\pm} pair production (opacity) was not taken into account because during the deceleration phase it is much less than unity ($\tau_{\gamma\gamma,\rm in} \ll 1$).

In general, we compute the SSC light curves for a stratified and a homogeneous medium at 10 and 100 GeV and compare them with the *Fermi*-LAT and MAGIC sensitivities. We show that, depending on the parameter values, the former are above the latter. We calculate the SSC light curves during the afterglow transition and show that for this transition to be well-identified, it is necessary not only to observe the synchrotron, but also the SSC emission. For instance, the SSC emission can help us to discriminate between the stratified-to-homogeneous afterglow transition and a reverse-shock scenario. We have computed the SED in the stratified and homogeneous media and also discussed their differences.

We emphasize that the equations of synchrotron flux are degenerate in parameters such that for an entirely distinct set of parameters the same results can be obtained. Therefore, this result is not unique, but it is a possible solution for GRB 190114C. It is worth noting that if the increase of the observed SSC flux around 400 s is not seen, then another set of parameters to describe GRB 190114C is required or an alternative scenario would have to be evoked.

Using the best-fit parameters reported for GRB 190114C, we have estimated the SSC light curves and fitted the SEDs for two epochs, 66–92 s and 0.2 day. We show that the SSC process could explain the VHE photons beyond the synchrotron limit in GRB 190114C.

Recently, Wang et al. (2019a) described the broadband SED of GRB 190114C with an SSC model for a homogeneous medium using the optical, X-ray, and LAT data between 50 s and 150 s. They concluded that the detection of sub-TeV photons is attributed to the large burst energy and low redshift. Derishev & Piran (2019) studied the physical conditions of the afterglow required for explaining the sub-TeV photons in GRB 190114C. These authors found that the Comptonization of X-ray photons at the border between the Thompson and KN regimes with a bulk and electron Lorentz factor of \simeq 100 and $\gamma_c \simeq 10^4$ could described the MAGIC detection. In our current work, in addition to studying the evolution of SSC light curves during the stratified-to-homogeneous afterglow transition as

¹² GRB 080916C, GRB 090510, GRB 090902B, GRB 090926A, GRB 110721A, GRB 110731A, GRB 130427A, GRB 160625B, and others (Abdo et al. 2009a, 2009b; Ackermann et al. 2010, 2011, 2013, 2014; Fraija et al. 2017a, 2017b).

 $[\]overline{^{13}}$ VERITAS started follow-up observations of GRB 130427A \sim 20 hr after the trigger time (Aliu et al. 2014).

reported in Fraija et al. (2019c), we have interpreted the photons beyond the synchrotron limit in the SSC framework and hence modeled its SED in the stratified and homogeneous media. We conclude that, although the photons beyond the synchrotron limit can be interpreted by the SSC process, the emission detected at hundreds of GeV is due to the closeness and the set of favorable parameter values of this burst. We conclude that low-redshift GRBs described under a favorable set of parameters as found in GRB 190114C could be detected at hundreds of GeV, and also afterglow transitions would allow VHE emission to be observed for longer periods. The results of our afterglow model in the homogeneous medium is consistent with the results reported in Derishev & Piran (2019). In our case, the SSC emission is below the KN regime, 868.1 GeV, with bulk and electron Lorentz factors of 101.2 and 1.9×10^{-4} , respectively. It is worth noting that the parameters obtained with the MCMC code from the broadband modeling of the multi-wavelength observations may change somewhat when the KN effects are considered, but the SSC emission itself will not be strongly affected.

We thank Xiang-Yu Wang and B.B Zhang for useful discussions. N.F. acknowledge financial support from UNAM-DGAPA-PAPIIT through Grant IA 102019. R.B.D. acknowledges support from the National Science Foundation under Grant 1816694.

Appendix

The proportionality constants in the stratified medium, Equation (4), are

$$\begin{split} F_{1,\mathrm{f}}^{\mathrm{W}} &\simeq 2.3 \, \times \, 10^{-5} \, \mathrm{mJy} \bigg(\frac{1 \, + \, Y_{\mathrm{Th}}}{3} \bigg)^{\frac{3}{3}} \bigg(\frac{1 \, + \, z}{1.5} \bigg)^{3} \\ &\quad \xi^{4} \varepsilon_{\mathrm{B},-4}^{\frac{5}{3}} \, A_{\mathrm{W},-1}^{-4} \, D_{27}^{-2} \, E_{53.5}^{-\frac{1}{3}}, \\ F_{2,\mathrm{f}}^{\mathrm{W}} &\simeq 2.1 \, \times \, 10^{-3} \, \mathrm{mJy} \bigg(\frac{1 \, + \, Y_{\mathrm{Th}}}{3} \bigg)^{-2} \bigg(\frac{1 \, + \, z}{1.5} \bigg)^{\frac{1}{2}} \\ &\quad \xi^{-\frac{1}{4}} \, \varepsilon_{\mathrm{B},-4}^{-\frac{5}{4}} \, D_{27}^{-2} \, A_{\mathrm{W},-1}^{\frac{1}{4}} \, E_{53.5}^{\frac{1}{2}}, \\ F_{3,\mathrm{f}}^{\mathrm{W}} &\simeq 2.5 \, \times \, 10^{-7} \, \mathrm{mJy} \, g(p)^{2(p-1)} \bigg(\frac{1 \, + \, Y_{\mathrm{Th}}}{3} \bigg)^{-2} \bigg(\frac{1 \, + \, z}{1.5} \bigg)^{\frac{p}{2}} \\ &\quad \xi^{\frac{p-2}{4}} \, \varepsilon_{\mathrm{B},-4}^{\frac{p-6}{4}} \, \varepsilon_{e,-2}^{2(p-1)} \, A_{\mathrm{W},-1}^{\frac{2-p}{4}} \, D_{27}^{-2} \, E_{53.5}^{\frac{p}{3}}, \\ F_{1,\mathrm{s}}^{\mathrm{W}} &\simeq 4.2 \, \times \, 10^{-2} \, \mathrm{mJy} \, g(p)^{-\frac{4}{3}} \bigg(\frac{1 \, + \, z}{1.5} \bigg)^{\frac{5}{3}} \\ &\quad \xi^{-\frac{8}{3}} \, \varepsilon_{\mathrm{B},-4}^{\frac{1}{3}} \, \varepsilon_{e,-2}^{-\frac{4}{3}} \, A_{\mathrm{W},-1}^{\frac{8}{3}} \, D_{27}^{-2} \, E_{53.5}^{-\frac{1}{3}}, \\ F_{2,\mathrm{s}}^{\mathrm{W}} &\simeq 8.6 \, \times \, 10^{-10} \, \mathrm{mJy} \, g(p)^{2(p-1)} \bigg(\frac{1 \, + \, z}{1.5} \bigg)^{\frac{p+3}{2}} \\ &\quad \xi^{\frac{p-11}{4}} \, \varepsilon_{\mathrm{B},-4}^{\frac{p+1}{4}} \, \varepsilon_{e,-2}^{2(p-1)} \, A_{\mathrm{W},-1}^{\frac{11-p}{4}} \, D_{27}^{-2} \, E_{53.5}^{\frac{p-1}{2}}, \\ \end{cases}$$

with $F_{3,s}^{W} = F_{3,f}^{W}$. The proportionality constants in the homogeneous medium, Equation (10), are

$$\begin{split} F_{1,\mathrm{f}}^{\mathrm{H}} &\simeq 2.3 \quad \times \quad 10^{-5} \, \mathrm{mJy} \bigg(\frac{1 + Y_{\mathrm{Th}}}{2.5} \bigg)^{\frac{4}{3}} \\ &\varepsilon_{\mathrm{B},-4}^{\frac{5}{3}} \, n^{-2} \, D_{27}^{-2} \, E_{53.5}^{\frac{5}{3}}, \\ F_{2,\mathrm{f}}^{\mathrm{H}} &\simeq 2.5 \quad \times \quad 10^{-6} \, \mathrm{mJy} \bigg(\frac{1 + Y_{\mathrm{Th}}}{2.5} \bigg)^{-2} \bigg(\frac{1 + z}{1.5} \bigg)^{\frac{3}{8}} \\ &\varepsilon_{\mathrm{B},-4}^{-\frac{5}{4}} \, D_{27}^{-2} \, n^{\frac{1}{8}} \, E_{53.5}^{\frac{5}{8}}, \\ F_{3,\mathrm{f}}^{\mathrm{H}} &\simeq 2.7 \quad \times \quad 10^{-10} \, \mathrm{mJy} \, g(p)^{2(1-p)} \bigg(\frac{1 + Y_{\mathrm{Th}}}{2.5} \bigg)^{-2} \bigg(\frac{1 + z}{1.5} \bigg)^{\frac{5p-2}{8}} \\ &\varepsilon_{\mathrm{B},-4}^{\frac{p-6}{8}} \, \varepsilon_{e,-2}^{2p-2} \, D_{27}^{-2} \, E_{53.5}^{\frac{3p+2}{8}}, \\ F_{1,\mathrm{s}}^{\mathrm{H}} &\simeq 4.6 \quad \times \quad 10^{-3} \, \mathrm{mJy} \, g(p)^{\frac{4}{3}} \bigg(\frac{1 + z}{1.5} \bigg)^{\frac{1}{3}} \\ &\varepsilon_{\mathrm{B},-4}^{\frac{1}{3}} \, \varepsilon_{e,-2}^{-\frac{4}{3}} \, n^{\frac{4}{3}} \, D_{27}^{-2} \, E_{53.5}, \\ F_{2,\mathrm{s}}^{\mathrm{H}} &\simeq 7.4 \quad \times \quad 10^{-11} \, \mathrm{mJy} \, g(p)^{2(p-1)} \bigg(\frac{1 + z}{1.5} \bigg)^{\frac{5p+1}{8}} \\ &\varepsilon_{\mathrm{B},-4}^{\frac{p+1}{4}} \, \varepsilon_{e,-2}^{2(p-1)} \, n^{\frac{11-p}{8}} \, D_{27}^{-2} \, E_{53.5}^{\frac{3p+7}{8}}, \\ \mathrm{with} \, F_{3,\mathrm{s}}^{\mathrm{H}} &= F_{3,\mathrm{f}}^{\mathrm{H}}. \end{split}$$

ORCID iDs

N. Fraija https://orcid.org/0000-0002-0173-6453 P. Beniamini https://orcid.org/0000-0001-7833-1043

References

Aartsen, M. G., Abraham, K., Ackermann, M., et al. 2016, ApJ, 824, 115

Aartsen, M. G., Ackermann, M., Adams, J., et al. 2015, ApJL, 805, L5

```
Abbasi, R., Abdou, Y., Abu-Zayyad, T., et al. 2012, Natur, 484, 351
Abdo, A. A., Ackermann, M., Ajello, M., et al. 2009a, ApJL, 706, L138
Abdo, A. A., Ackermann, M., Arimoto, M., et al. 2009b, Sci, 323, 1688
Abeysekara, A. U., Aguilar, J. A., Aguilar, S., et al. 2012, APh, 35, 641
Abeysekara, A. U., Archer, A., Benbow, W., et al. 2018, ApJ, 857, 33
Acciari, V. A., Aliu, E., Arlen, T., et al. 2011, ApJ, 743, 62
Ackermann, M., Ajello, M., Asano, K., et al. 2011, ApJ, 729, 114
Ackermann, M., Ajello, M., Asano, K., et al. 2013, ApJ, 763, 71
Ackermann, M., Ajello, M., Asano, K., et al. 2013, ApJS, 209, 11
Ackermann, M., Ajello, M., Asano, K., et al. 2014, Sci, 343, 42
Ackermann, M., Asano, K., Atwood, W. B., et al. 2010, ApJ, 716, 1178
Aharonian, F., Akhperjanian, A. G., Barres de Almeida, U., et al. 2009a, A&A,
   495, 505
Aharonian, F., Akhperjanian, A. G., Barres DeAlmeida, U., et al. 2009b, ApJ,
  690, 1068
Ajello, M., Arimoto, M., Axelsson, M., et al. 2019, ApJ, 878, 52
Albert, J., Aliu, E., Anderhub, H., et al. 2007, ApJ, 667, 358
Aleksić, J., Ansoldi, S., Antonelli, L. A., et al. 2014, MNRAS, 437, 3103
Alexander, K. D., Laskar, T., Berger, E., Mundell, C. G., & Margutti, R. 2019,
   GCN, 23726, 1
Aliu, E., Aune, T., Barnacka, A., et al. 2014, ApJL, 795, L3
Asano, K., Guiriec, S., & Mészáros, P. 2009, ApJL, 705, L191
Barniol Duran, R., & Kumar, P. 2011, MNRAS, 412, 522
Bartoli, B., Bernardini, P., Bi, X. J., et al. 2017, ApJ, 842, 31
Beniamini, P., Nava, L., Duran, R. B., & Piran, T. 2015, MNRAS, 454, 1073
Beniamini, P., Nava, L., & Piran, T. 2016, MNRAS, 461, 51
Beniamini, P., & van der Horst, A. J. 2017, MNRAS, 472, 3161
```

```
Bolmer, J., & Shady, P. 2019, GCN, 23702, 1
Chevalier, R. A., & Li, Z.-Y. 2000, ApJ, 536, 195
Chevalier, R. A., Li, Z.-Y., & Fransson, C. 2004, ApJ, 606, 369
Dai, Z. G., & Lu, T. 1998, MNRAS, 298, 87
D'Avanzo, P., Covino, S., Fugazza, D., & Melandri, A. 2019, GCN, 23729, 1
de Ugarte Postigo, A., Kann, D. A., Thoene, C. C., & Izzo, L. 2019, GCN,
   23692, 1
Derishev, E., & Piran, T. 2019, ApJL, 880, 27
Dermer, C. D., Böttcher, M., & Chiang, J. 2000, ApJ, 537, 255
Fraija, N. 2014, MNRAS, 437, 2187
Fraija, N., De Colle, F., Veres, P., et al. 2019a, ApJ, 871, 123
Fraija, N., De Colle, F., Veres, P., et al. 2019b, arXiv:1906.00502
Fraija, N., Dichiara, S., Pedreira, A. C. C. d. E. S., et al. 2019c, ApJL, 879, L26
Fraija, N., Dichiara, S., Pedreira, A. C. C. d. E. S., et al. 2019d, arXiv:1905.
Fraija, N., González, M. M., & Lee, W. H. 2012, ApJ, 751, 33
Fraija, N., Lee, W., & Veres, P. 2016a, ApJ, 818, 190
Fraija, N., Lee, W. H., Araya, M., et al. 2017a, ApJ, 848, 94
Fraija, N., Lee, W. H., Veres, P., & Barniol Duran, R. 2016b, ApJ, 831, 22
Fraija, N., Lopez-Camara, D., Pedreira, A. C. C. d. E. S., et al. 2019e,
   arXiv:1904.07732
Fraija, N., Pedreira, A. C. C. d. E. S., & Veres, P. 2019f, ApJ, 871, 200
Fraija, N., & Veres, P. 2018, ApJ, 859, 70
Fraija, N., Veres, P., Zhang, B. B., et al. 2017b, ApJ, 848, 15
Franceschini, A., & Rodighiero, G. 2017, A&A, 603, A34
Frederiks, D., Golenetskii, S., Aptekar, R., et al. 2019, GCN, 23737, 1
Funk, S., & Hinton, J. 2013, APh, 43, 348
Funk, S., Hinton, J. A. & CTA Consortium 2013, APh, 43, 348
Ghisellini, G., Ghirlanda, G., Nava, L., & Celotti, A. 2010, MNRAS, 403, 926
Gould, R. J., & Schréder, G. 1966, PhRvL, 16, 252
Gropp, J. D., Kennea, J. A., Klingler, N. J., et al. 2019, GCN, 23688, 1
H.E.S.S. Collaboration, Abramowski, A., Aharonian, F., et al. 2014, A&A,
   565, A16
Hurley, K., Dingus, B. L., Mukherjee, R., et al. 1994, Natur, 372, 652
Im, M., Paek, G. S., Kim, S., Lim, G., & Choi, C. 2019a, GCN, 23717, 1
Im, M., Paek, G. S. H., & Choi, C. 2019b, GCN, 23740, 1
Izzo, L., Noschese, A., D'Avino, L., & Mollica, M. 2019, GCN, 23699, 1
Kobayashi, S. 2000, ApJ, 545, 807
Kocevski, D., Omodei, N., Axelsson, M., et al. 2019, GCN, 23709, 1
Kumar, P., & Barniol Duran, R. 2009, MNRAS, 400, L75
```

Kumar, P., & Barniol Duran, R. 2010, MNRAS, 409, 226

Laskar, T., Alexander, K. D., Gill, R., et al. 2019, ApJ, 878, 26

Lipunov, V., Tyurina, N., Kuznetsov, A., et al. 2019, GCN, 23693, 1

```
Liu, R.-Y., Wang, X.-Y., & Wu, X.-F. 2013, ApJL, 773, L20
Longo, F., Bissaldi, E., Vianello, G., et al. 2016, GCN, 19413, 1
Mazaeva, E., Pozanenko, A., Volnova, A., Belkin, S., & Krugov, M. 2019,
  GCN, 23741, 1
Mészáros, P., & Rees, M. J. 2000, ApJL, 541, L5
Minaev, P., & Pozanenko, A. 2019, GCN, 23714, 1
Mirzoyan, R., Noda, K., Moretti, E., et al. 2019, GCN, 23701, 1
Nakar, E., Ando, S., & Sari, R. 2009, ApJ, 703, 675
Nava, L., Vianello, G., Omodei, N., et al. 2014, MNRAS, 443, 3578
Osborne, J. P., Beardmore, A. P., Evans, P. A., & Goad, M. R. 2019, GCN,
  23704, 1
Panaitescu, A., & Kumar, P. 2000, ApJ, 543, 66
Panaitescu, A., & Mészáros, P. 2000, ApJL, 544, L17
Panaitescu, A., Vestrand, W. T., & Woźniak, P. 2014, ApJ, 788, 70
Papathanassiou, H., & Meszaros, P. 1996, ApJL, 471, L91
Piran, T., & Nakar, E. 2010, ApJL, 718, L63
Piron, F. 2016, CRPhy, 17, 617
Planck Collaboration, Aghanim, N., Akrami, Y., et al. 2018, arXiv:1807.06209
Ravasio, M. E., Oganesyan, G., Salafia, O. S., et al. 2019, A&A, 626, 12
Sacahui, J. R., Fraija, N., González, M. M., & Lee, W. H. 2012, ApJ, 755, 127
Santana, R., Barniol Duran, R., & Kumar, P. 2014, ApJ, 785, 29
Sari, R., & Esin, A. A. 2001, ApJ, 548, 787
Sari, R., Piran, T., & Narayan, R. 1998, ApJL, 497, L17
Selsing, J., Fynbo, J. P. U., Heintz, K. E., & Watson, D. 2019, GCN, 23695, 1
Siegel, M. H., & Gropp, J. D. 2019, GCN, 23725, 1
Takahashi, K., Murase, K., Ichiki, K., Inoue, S., & Nagataki, S. 2008, ApJL,
Tyurina, N., Lipunov, V., Kuznetsov, A., et al. 2019, GCN, 23690, 1
Ursi, A., Tavani, M., Marisaldi, M., et al. 2019, GCN, 23712, 1
Vandenbroucke, J. 2019, ATel, 12395, 1
Vedrenne, G., & Atteia, J.-L. 2009, Gamma-Ray Bursts (Berlin: Springer)
Veres, P., & Mészáros, P. 2012, ApJ, 755, 12
Vink, J. S., & de Koter, A. 2005, A&A, 442, 587
Vink, J. S., de Koter, A., & Lamers, H. J. G. L. M. 2000, A&A, 362, 295
Wang, X. Y., Dai, Z. G., & Lu, T. 2001, ApJL, 546, L33
Wang, X.-Y., He, H.-N., Li, Z., Wu, X.-F., & Dai, Z.-G. 2010, ApJ, 712, 1232
Wang, X.-Y., Liu, R.-Y., & Lemoine, M. 2013, ApJL, 771, L33
Wang, X.-Y., Liu, R.-Y., Zhang, H.-M., Xi, S.-Q., & Zhang, B. 2019a,
  arXiv:1905.11312
Wang, Y., Li, L., Moradi, R., & Ruffini, R. 2019b, arXiv:1901.07505
Xiao, S., Li, C. K., Li, X. B., et al. 2019, GCN, 23716, 1
Zhang, B., & Mészáros, P. 2001, ApJ, 559, 110
Zou, Y.-C., Fan, Y.-Z., & Piran, T. 2009, MNRAS, 396, 1163
```